mater.scichina.com link.springer.com Published online 19 March 2024 | https://doi.org/10.1007/s40843-023-2847-1
Sci China Mater 2024, 67(4): 1101–1123

SPECIAL TOPIC: Computation-assisted Materials Screening and Design

Recent progress on catalyst design of nitrogen reduction reaction by density functional theory

Tian-Yi Dai, Chun-Cheng Yang* and Qing Jiang*

ABSTRACT The electrochemical nitrogen reduction reaction (NRR) technique has great potential for alleviating the high fossil fuel consumption and carbon emissions of the industrial Haber-Bosch method for ammonia (NH_3) synthesis. Moreover, the NRR provides great prospects for fully exploiting renewable energy since NH_3 is a promising energy carrier without carbon emissions. However, the development of the NRR technique is limited by the lack of efficient catalysts. Great efforts have been made to develop high-efficiency catalysts thus far, in which density functional theory (DFT) calculations have played an important role in assisting catalyst design. Herein, we summarize the recent catalyst design strategies to boost the NRR performance, i.e., the activity and selectivity. Additionally, representative computational studies are reviewed, accompanied by insights into further improving the catalytic behavior. Finally, we briefly discuss the challenges and opportunities in catalyst design *via* DFT calculations. The purpose of this review is to motivate more intelligent design strategies for high-efficiency NRR.

Keywords: nitrogen reduction reaction, density functional theory, materials design, two-dimensional materials, machine learning

INTRODUCTION

Ammonia (NH_3) is one of the most important chemicals in the world, and its annual output exceeds 200 million tons globally, with a market value of over USD $70 billion [1]. Approximately 80% of the produced NH_3 is utilized for producing fertilizers, and the remainder is used as an industrial refrigerant or a chemical feedstock for producing explosives, plastics, synthetic fibres, resins, and so on [2–5]. Moreover, owing to its high hydrogen content (17.8 wt%) and high energy content (5.2 kW h kg^{-1}), NH_3 is also considered a promising energy carrier with zero carbon emissions [6,7]. That is, NH_3 is not only a strong candidate for a hydrogen carrier but also can be directly used as a fuel for internal combustion engines and fuel cells [8,9]. Moreover, the existing technologies for NH_3 liquefaction, storage and transport are well established; thus, NH_3 is an ideal energy carrier [1,10].

The industrial production of NH_3 is currently dominated by the Haber-Bosch method, in which N_2 and H_2 directly react to produce NH_3 ($N_2 + 3H_2 \rightleftharpoons 2NH_3$, $\Delta H^{\ominus}_{298\,K} = -45.9$ kJ mol^{-1}) [11]. This reaction requires a high temperature (300–500°C) to overcome the sluggish kinetics and a high pressure (200–300 bar, 1 bar = 10^5 Pa) to shift the equilibrium towards NH_3 production. Therefore, the Haber-Bosch process can only run in substantial centralized infrastructures that can maintain harsh reaction conditions [12,13]. Moreover, the H_2 feedstocks are produced from fossil fuels, including natural gas, coal and petroleum, with strong energy demands of 7.8, 10.6, and 11.7 MW h per ton of NH_3, respectively [14,15]. In addition, the corresponding CO_2 emissions are 1.6, 3.0, and 3.8 tons per ton of NH_3, which are very harmful to the environment. As a result, the Haber-Bosch method consumes approximately 2% of the global energy supply and generates more than 300 million metric tons of carbon dioxide (CO_2) annually [16–18]. It is widely known that fossil fuel reserves are limited and will be depleted in the future, while CO_2 emissions cause climate change and bring about extreme weather events [19]. Therefore, the century-old NH_3 synthesis technology urgently needs to be transformed to be environmentally friendly to eliminate dependence on fossil fuels. This goal presents new challenges for basic science and engineering research.

Green NH_3 synthesis powered by renewable electricity reduces the CO_2 emissions in NH_3 production. One of the routes is to combine water electrolysis technology for H_2 production with the established Haber-Bosch factories. The energy consumption in this route is suggested to be 10–12 MW h per ton of NH_3 [14]. Nonetheless, the intermittency of renewable energy sources (except for hydro and geothermal sources) causes difficulties in the continuous operation of the Haber-Bosch process, and thus additional energy storage devices are required. Another route of green NH_3 synthesis is to directly produce NH_3 *via* the electrochemical nitrogen reduction reaction (NRR), which can be performed under mild conditions with a H source supplied by water [11,20]. This route is well suited for a distributed farm economy rather than substantial centralized infrastructures, is thus a good match for intermittent renewable energy and alleviates the need for significant H_2O feedstock [21]. In particular, electrochemical devices can potentially realize direct utilization of seawater without the need for desalination, and the H_2O feedstock for the NRR can thus be abundantly supplied [22]. The entire process involves zero carbon emissions [13,23]. Moreover, given that NH_3 is an ideal energy carrier, electrochemical NH_3 synthesis also provides a promising energy storage approach for recycling off-peak electrical power. In summary, the develop-

Key Laboratory of Automobile Materials, Ministry of Education, and School of Materials Science and Engineering, Jilin University, Changchun 130022, China
* Corresponding authors (emails: ccyng@jlu.edu.cn (Yang CC); jiangq@jlu.edu.cn (Jiang Q))

ment of electrochemical NH_3 synthesis technology can not only alleviate the high fossil fuel consumption of the Haber-Bosch method but also complement the existing energy system.

One of the priorities in realizing electrochemical NH_3 synthesis is to explore efficient electrocatalysts for the NRR. In addition, other approaches can further improve the NRR activity and selectivity, such as optimizing the electrolyzer, improving the N_2 solubility and selecting appropriate electrolyte. Density functional theory (DFT) calculations, which are based on the electron density of atoms, are acknowledged as powerful tools for assisting in material design [24–26]. At present, the state-of-the-art DFT calculations can not only describe the electronic interactions of catalytic sites but also reveal the mechanisms underlying catalytic reactions [27–30]. Therefore, DFT calculations provide a fundamentals-based bottom-up approach for the design of materials with high performance and good stability [31]. In the past few years, great efforts have been made to develop innovative materials for the electrocatalytic NRR [32–36]. Early on, Rod *et al.* [37] thoroughly studied the NRR process on Ru(0001) *via* DFT calculations. They first proposed the possible reaction pathway of the NRR and discussed the selectivity between the NRR and the hydrogen evolution reaction (HER). The high NRR activity and preferential selectivity of Ru(0001) were subsequently verified by experimental studies [38,39]. Skúlason *et al.* [40] established a catalytic volcano plot of the NRR on pure transition metals (TMs), which has become an important guideline for catalyst design. Our group theoretically proposed that MoB_2 can be a high-efficiency NRR catalyst [41]. The remarkable NRR performance of MoB_2 was further confirmed by a proof-of-concept experiment, which successfully bridged the gap between theory and experiment. These studies suggest that theoretical computations can assist in the discovery of new catalyst materials.

In this review, we summarize recent theoretical progress in the design of materials for highly efficient electrochemical NRR. Herein, we first introduce the fundamental understanding of the NRR from a theoretical perspective, including the possible reaction mechanisms, as well as the advances and bottlenecks at this stage. Then, we present rational material design strategies for achieving high activity and high selectivity for the NRR and review representative computational studies. Finally, we briefly discuss the existing challenges and future opportunities in this research field.

FUNDAMENTALS OF THE CATALYTIC NRR

The electrochemical NRR is a complex process involving six proton-electron transfer steps and multiple intermediates, which results in great difficulties in exploring the reaction mechanisms [42]. Moreover, the NRR yields still do not satisfy the standards for practical applications due to limitations in the activity and selectivity [43,44]. The industrialization standard of the NH_3 yield is up to 6120 $\mu g\ h^{-1}\ cm^{-2}$, with a Faradaic efficiency (FE) of up to 50% [45]. The above points are briefly presented in this section.

Reaction mechanisms

Several possible NRR mechanisms have been established based on theoretical studies, which mainly include the dissociative mechanism, the associative mechanism and the Mars-van Krevelen (MvK) mechanism [45]. In the dissociative mechanism, N_2 molecules are first split into two N atoms on the catalyst surface, and then, the N atoms are independently hydrogenated. The dissociative mechanism is similar to that in the industrial Haber-Bosch method and requires a high activation energy to cleave the stable N≡N triple bond. In contrast, in the associative mechanism, the N_2 molecules are hydrogenated step by step, and the N≡N bond is continuously cleaved and finally broken, with the release of NH_3 [35]. At present, most catalysts preferentially exhibit the associative mechanism in the electrochemical NRR since direct cleaving of the N≡N triple bond is extremely difficult under mild conditions. Nonetheless, rational catalyst design is promising for obtaining a low energy barrier for N_2 dissociation, in which case the dissociative mechanism may be the dominant mechanism [46]. Therefore, both the dissociative mechanism and associative mechanism should be considered in a catalyst system.

The associative mechanism can be further classified into four possible pathways according to the different initial adsorption configurations of N_2 molecules on the active sites: the distal and alternating pathways for an end-on adsorption configuration of N_2 and consecutive and enzymatic pathways for a side-on adsorption configuration of N_2. In the distal pathway (Fig. 1a), hydrogenation first occurs for the N atom away from the active site. It successively generates NNH^*, NNH_2^* and NNH_3^* intermediates, and the first NH_3 molecule is released with the N–N bond breaks. Subsequently, the remaining N atom on the active site continues to hydrogenate, successively generating NH^*, NH_2^* and NH_3^* intermediates and eventually releasing the second NH_3 molecule. In the alternating pathway (Fig. 1b), the two N atoms of N_2 are alternately hydrogenated to produce NNH^*, $NHNH^*$, $NHNH_2^*$ and $NH_2NH_2^*$ intermediates, which successively generate two NH_3 molecules in the following steps. For the side-on adsorption configuration of N_2, the consecutive pathway (Fig. 1c) is analogous to the distal pathway, i.e., hydrogenation first occurs on one of the N atoms and then on the other N atom after the release of the first NH_3 molecule. The enzymatic pathway (Fig. 1d) is similar to the alternating pathway, in which two N atoms are alternately hydrogenated, and the two NH_3 molecules are successively released.

The MvK mechanism is possible on transition metal nitrides (TMNs) and transition metal carbides (TMCs) [47]. In this mechanism, an N atom on the lattice is first reduced to NH_3, which is released, with a vacancy left on the catalyst surface. Then, the vacancy is refilled by the capture of a new N_2 molecule, which is further reduced to the second NH_3 molecule. Recently, a surface hydrogenation mechanism was proposed in which H^+ ions are first adsorbed on catalyst surfaces, and then, the N_2 molecule directly reacts with two adsorbed H^* ions to form an $NHNH^*$ intermediate [48]. The subsequent steps are akin to the enzymatic pathway, which involves the formation of $NHNH_2^*$ and $NH_2NH_2^*$ intermediates and the sequential release of two NH_3 molecules. These two NRR pathways bypass the hard N_2 activation step, thus effectively alleviating the high overpotentials of the associative mechanism.

Activity challenges

N_2 is often used as a protective gas due to the high dissociation energy of the N≡N bond (941 kJ mol^{-1}). The extraordinary stability of the N_2 molecule can also be attributed to the high cleavage energy of the first bond in N≡N (410 kJ mol^{-1}) [13], leading to much greater stability of N_2 than that of other triple-bonded molecules, such as acetylene (HC≡CH, with dissociation

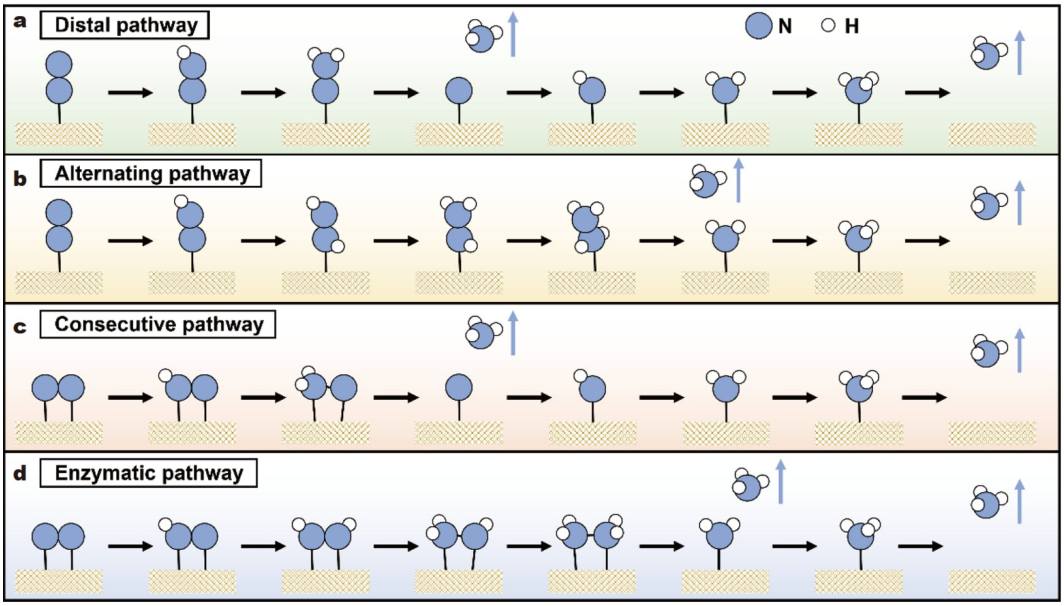

Figure 1 Schematic illustration of the NRR reaction pathways. (a) Distal pathway. (b) Alternating pathway. (c) Consecutive pathway. (d) Enzymatic pathway.

energy of 962 kJ mol^{-1} but with a low cleavage energy of the first bond of 222 kJ mol^{-1} [49]). In addition, the large energy gap between the highest occupied and lowest unoccupied molecular orbitals (10.82 eV) of the N_2 molecule hinders electron transfer. Thus, N_2 is relatively inert for chemical interactions [50].

The molecular orbital diagram of N_2 is shown in Fig. 2a, where the N≡N bond is generated by the hybridization of 2p orbitals of two N atoms, with three antibonding orbitals (σ^* and π^* orbitals) generated at the same time [51]. During the chemisorption of N_2 onto TM atoms, the empty d orbitals of the TMs accept the lone-pair electrons of N_2, and the occupied d orbitals of the TMs donate electrons to the π^* orbitals of N_2. The entire electron transfer process is called the "acceptance-donation" mechanism (Fig. 2b) [52]. The acceptance mechanism stabilizes the adsorption of N_2 onto the active site, while the donation mechanism fills the antibonding orbitals of N_2 and thus weakens the N≡N bond.

The prerequisite for the "acceptance-donation" mechanism is the coexistence of empty and occupied orbitals at active sites. TM-based catalysts, such as Fe ($3d^6$) and Ru ($4d^7$), fit this requirement well and are thus widely used in industrial Haber-Bosch methods for NH_3 synthesis [53,54]. Interestingly, the nonmetal element B ($2p^1$) can also mimic the "acceptance-donation" process, where the empty sp^2 orbitals of B work for the "acceptance" process and the occupied p orbitals of B affect the "donation" process [55,56]. Unlike TM-based catalysts, B atoms can prohibit the binding of Lewis acid protons in electrolytes, resulting in B simultaneously promoting the NRR and inhibiting the HER [57]. A further requirement for the "acceptance-donation" mechanism is good matching of electronic orbitals in terms of both energy and symmetry [58]. It is plausible that the N_2 in a side-on adsorption configuration is better activated than that in an end-on configuration, since the π^* orbitals of side-on N_2 better match the occupied orbitals of TMs and thus receive more electrons in the "donation" process [59].

The challenges associated with the NRR activity can also be attributed to the existence of scaling relations. That is, the adsorption energies of intermediates on catalyst surfaces linearly scale with each other. Scaling relations can describe the trends of the adsorption energies and reaction energies of several catalyst systems, which is helpful for predicting the catalytic activity of similar systems. Nonetheless, the scaling relations also impose an inherent limit on the catalytic activity. An ideal NRR process should involve strong binding of N_2 to guarantee effective N_2 activation but weak adsorption of $*NH_z$ (z = 1, 2) intermediates to promote their further hydrogenation [60]. It is extremely difficult for one catalyst to simultaneously satisfy these two types of requirements. Thus, moderate adsorption is suggested. In this case, the NRR activity can at most achieve the highest values described by volcano plots, while this activity is still unsatisfactory compared with the industrialized standard. At present, the NRR activity is evaluated by the limiting potential (U_L), where a smaller absolute value of U_L indicates higher intrinsic catalytic activity of a catalyst. To address the activity challenges of the NRR, scaling relations should be avoided, and low U_L values should be obtained.

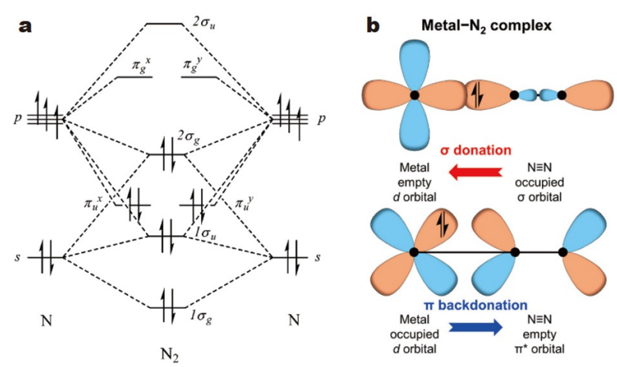

Figure 2 (a) Schematic diagrams of N_2 molecular orbitals. Reprinted with permission from Ref. [51]. Copyright 2014, The Royal Society of Chemistry. (b) "Acceptance-donation" mechanism for N_2 activation. Reprinted with permission from Ref. [52]. Copyright 2022, American Chemical Society.

Selectivity challenges

In aqueous solutions, the NRR is severely hampered by the competitive HER, which involves only two proton-electron transfer steps and is kinetically more favourable [61]. A further understanding of the competition between the NRR and HER is based on the fact that the rate of the NRR is zeroth-order in the proton and electron concentrations, while that of the HER is first-order in both [44]. That is, as the proton and electron concentrations in the solution increase, the reaction rate of the HER also increases, while the effect on the NRR is negligible [62]. Moreover, owing to the quite low solubility of N_2 in electrolytes, the active sites are easily occupied by the large amount of protons. Overall, all of the above issues present great challenges for NRR selectivity. A low NRR selectivity increases the cost of NH_3 production due to the large waste of electrical power on the HER. As a result, an effective strategy for suppressing the HER is urgently required.

The selectivity of the NRR can be evaluated by the FE value, which describes the percentage of charge transferred to the NRR in the whole system. A higher FE indicates better selectivity for the NRR [63]. Thus far, several experimental strategies have been proposed to improve the NRR selectivity, such as using a nonaqueous solution or adding a hydrophobic layer onto the catalyst surface to block protons, through which the adsorption of N_2 can be greatly improved [64,65]. From a theoretical perspective, the preferential adsorption of N_2 over that of protons is required for NRR catalysts, where the adsorption free energies of N_2 $\left(\Delta G_{N_2^*}\right)$ and H^+ (ΔG_{H^*}) on the active sites should be compared in a computation work. However, since the adsorption of H^+ involves both proton and electron transfer, it is promoted by the negative electrode potential under reducing conditions [66]. In contrast, the adsorption of N_2 without proton or electron transfer is insensitive to the electrode potential. Therefore, the $\Delta G_{N_2^*}$ on active sites should be much greater than ΔG_{H^*} to obtain a high FE value.

STRATEGIES TO IMPROVE THE ACTIVITY

The catalytic activity of a catalyst is determined by the number and intrinsic activity of the active sites, which can be improved *via* rational material design. DFT calculations are powerful tools for exploring interactions at the atomic level and accurately describing electronic properties. By performing DFT calculations, both regulation of the electronic structures of active sites and prediction of new reaction mechanisms as efficient strategies to improve the NRR activity can be realized [67]. In this section, these strategies for the NRR are summarized.

Regulating the interactions between active sites and substrates

Regulation of the interactions between active sites and substrates is an effective strategy. It can not only contribute to the stability of the catalyst, but also optimize the electronic structure of the active sites to further improve the performance [68]. Two-dimensional (2D) materials as substrates have attracted great attention due to their large specific surface area, high mechanical strength and fast electron transport [68,69]. The uniformly distributed pores on the basal surface of 2D materials are natural sites for sustaining active single atoms or clusters, and the confinement effect of these pore structures further contributes to the stability of the catalysts. Moreover, the preparation techniques of 2D materials are very facile, and surface engineering is facilely achievable due to the large fraction of surface atoms; thus, further improvement of the conductivity or the formation of more active sites can be easily realized [70]. In particular, the 2D geometric structure provides an ideal model for establishing a bridge between theory and experiment, which is very favourable for optimizing the catalytic behavior by modifying the electronic structure [71].

Carbon-based materials are widely used in electrocatalysis due to their excellent conductivity, easy fabrication and low cost [72]. Moreover, N-decorated carbon-based materials can not only exhibit improved charge mobility but also provide stable binding sites for good dispersion of TM atoms [73]. Our group has explored the NRR performance of a series of N-doped graphene-supported double-atom catalysts (DACs) [74]. The structure of a DAC is illustrated in Fig. 3a, where the active centres are composed of two TM atoms with six coordinated N atoms. Owing to the stable chemical bonding between the TMs and N atoms, these DACs exhibit good stability, as confirmed by the binding energy calculations shown in Fig. 3b. Moreover, the coordinated N atoms modify the electronic structures of the TM atoms, and the DACs thus possess high intrinsic activity for the NRR. Through a thorough computational screening of the catalytic activity for the NRR, VFe-N-C was identified as the optimal catalyst. Guo *et al.* [75] also proposed 2D expanded phthalocyanine (Pc) as a substrate for supporting DACs, where the active centres are M_2-N_6 moieties. They explored the thermodynamic and electrochemical stabilities of the catalysts by computing the formation energy and the dissolution potential (Fig. 3c), in which only 5 of 30 candidates were ruled out, indicating the high stability of the Pc substrate. They further screened for the best catalyst, V_2-Pc, whose U_L value was −0.39 V *vs.* reversible hydrogen electrode (RHE). The electronic structure of N_2 on V_2-Pc is illustrated in Fig. 3d, where the N_2 and V orbitals are well hybridized with each other. The electrons of V are transferred to N_2, and thus, the antibonding states of N_2 are located below the Fermi level, effectively weakening the N≡N bond.

Stacked heterostructures of 2D materials, based on van der Waals interactions between layers, were proposed as stable substrates to effectively prevent metal atoms from dissolving and aggregating. Graphdiyne (GDY) is a 2D carbon allotrope with an ordered porous geometry, in which sp-hybridized C atoms can stably bond to external TM atoms *via* strong d-π interactions [76]. The band gap (~1.2 eV) of GDY hampers electron transport in electrocatalysis, while the stacked heterostructure of GDY and single-layer graphene (GDY/Gra) can realize improved conductivity and good stability, and can thus serve as a substrate material to support Fe atoms for the NRR [70]. The structures of Fe_x-GDY/Gra are shown in Fig. 4a, where active centres with different atomic numbers are proposed. Fe_x-GDY/Gra exhibits metallic characteristics in the density of states (DOS), which confirms the excellent conductivity of the GDY/Gra heterostructure. Moreover, Fe_x-GDY/Gra exhibits high stability since Fe atoms are tightly confined to the pores of GDY/Gra, which is demonstrated by the computed results of strong binding energies in the thermodynamics (Fig. 4b) and ultrahigh diffusion barriers in the kinetics (Fig. 4c). Owing to the high stability of GDY/Gra, the ultimate theoretical mass loading of Fe atoms reaches 35.8 wt% when all the pores of GDY are covered. The NRR process on Fe_3-GDY/Gra-35.8 is shown in Fig. 4d, which follows the consecutive pathway with a low U_L

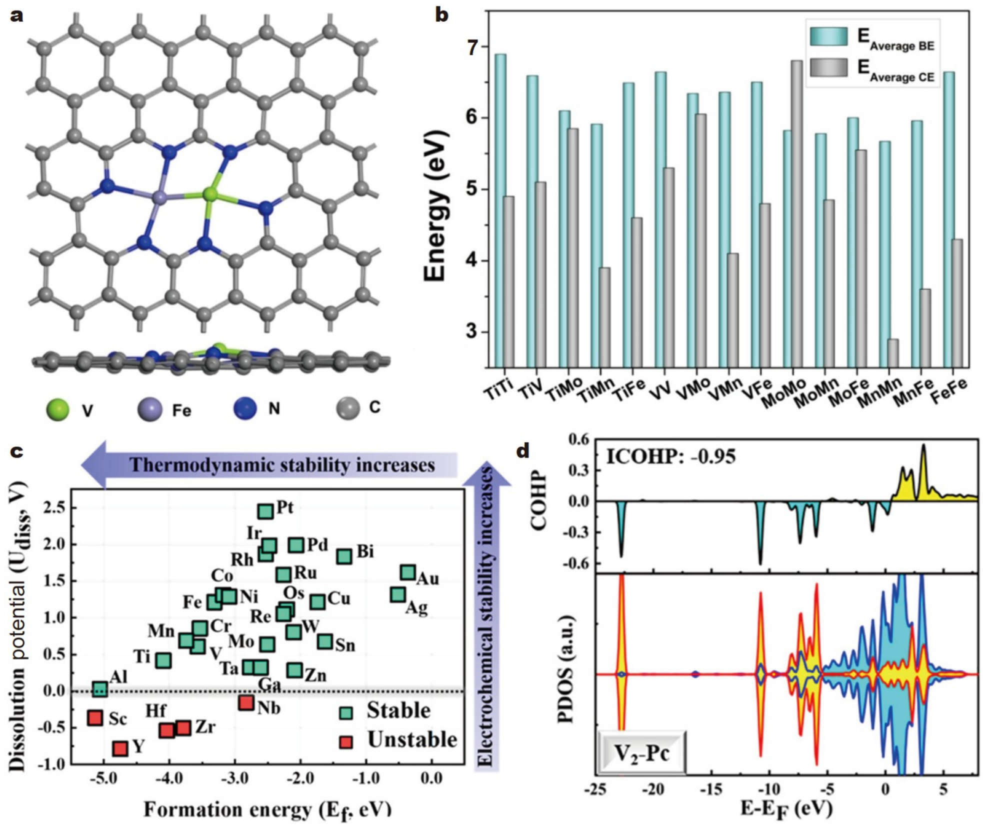

Figure 3 (a) Structural illustration of VFe-N-C from the top and side views. (b) Comparison of the average binding energies and average cohesive energies of a single TM atom in DACs and the bulk phase. Reprinted with permission from Ref. [74]. Copyright 2021, Wiley-VCH. (c) Computed formation energy and dissolution potential of TM atoms in M_2-Pc. (d) Crystal orbital Hamilton populations (COHPs) and partial DOS (PDOS) of N_2 on V_2-Pc. Reprinted with permission from Ref. [75]. Copyright 2020, American Chemical Society.

value (−0.26 V *vs*. RHE), denoting a high NRR performance. Deng *et al*. [77] proposed a strategy of encapsulating metal atoms into the interlayer of 2D material heterostructures to greatly enhance the stability of catalysts. In light of this strategy, Tang *et al*. [78] proposed a heterostructure of a single TM atom sandwiched between hexagonal boron nitride (h-BN) and graphene (BN/TM/G, Fig. 4e), where the TM atom exhibited a strong binding energy and a high diffusion barrier as expected. Interestingly, the active sites are no longer the trapped TM atoms but the B atoms on the h-BN surface with modified electronic structures. The N_2 molecule is activated at the B sites, as shown in Fig. 4f. The PDOS illustrates (Fig. 4g) that the empty p_z orbitals of B accept the lone-pair electrons of N_2, and the occupied p_z orbitals of B donate electrons to the π* orbitals of N_2 and weaken the N≡N triple bond. Thus, a facile NRR process on BN/TM/G is realized.

2D materials with covalently bonded atomic layers possess intrinsic stabilities and are powerful candidates for substrates. A typical representative is MoS_2, which has attracted significant attention due to its high catalytic activity and good stability [79]. Azofra *et al*. [80] proposed the use of single Fe atom-doped MoS_2 to mimic the active moiety in the nitrogenase of an Fe-Mo-S cofactor (Fig. 5a), which successfully realized conversion of N_2 to NH_3 with high selectivity. Owing to the rigid configuration of 2D materials with covalent bonds between the layers, they are very suitable for supporting atomic clusters. It is proposed that the synergistic effect of atomic clusters can enhance the "donation" process to N_2-π* orbitals for robust N_2 activation (Fig. 5b); thus, an Fe_4 cluster catalyst anchored to the 2D GaS surface was developed for catalysing the NRR (Fig. 5c) [58]. Owing to the strong N_2 activation, the first step of the NRR process on Fe_4/GaS is very facile. Moreover, 2D materials of this type can be solely used for catalysing the NRR since surface defects and edge sites with extra dangling bonds can strongly activate N_2 [81]. In addition, with a rational catalyst design strategy, the density of intrinsic defects is even greater than that in TM-doped materials, which indicates the potential of 2D materials as high-efficiency NRR catalysts [82].

Transition metal oxides (TMOs) are promising substrates since they are nontoxic, abundant and stable, and show poor activity for the HER. Gao *et al*. [83] reported the Nb single-atom-decorated anatase TiO_2(110) for the NRR (Fig. 6a). The PDOS in Fig. 6b illustrates that Nb atom doping can increase the electron density at the Fermi level, thus improving the electrical conductivity. Moreover, the Nb site on TiO_2(110) shows a lower Δ*G* of the PDS than pristine TiO_2(110), demonstrating that Nb doping on TiO_2(110) can enhance the NRR performance (Fig. 6c). Huang *et al*. [84] proposed a strategy to boost N_2 activation on MnO_2 surfaces *via* Fe doping. N_2 molecules can be stably adsorbed on the Fe–Mn bridge sites with the reception of electrons (Fig. 6d). As a result, the Δ*G* of the PDS on Fe-MnO_2 is 0.13 eV greater than that on pristine MnO_2 (Fig. 6e). Jin *et al*. [85] prepared a catalyst with a core-shell nanostructure by coating polypyrrole (PPy) onto S-doped Fe_2O_3 nanoparticles, which was denoted as S-Fe_2O_3@PPy (Fig. 6f). DFT calculations demonstrated that the synergistic effect of the S doping and the

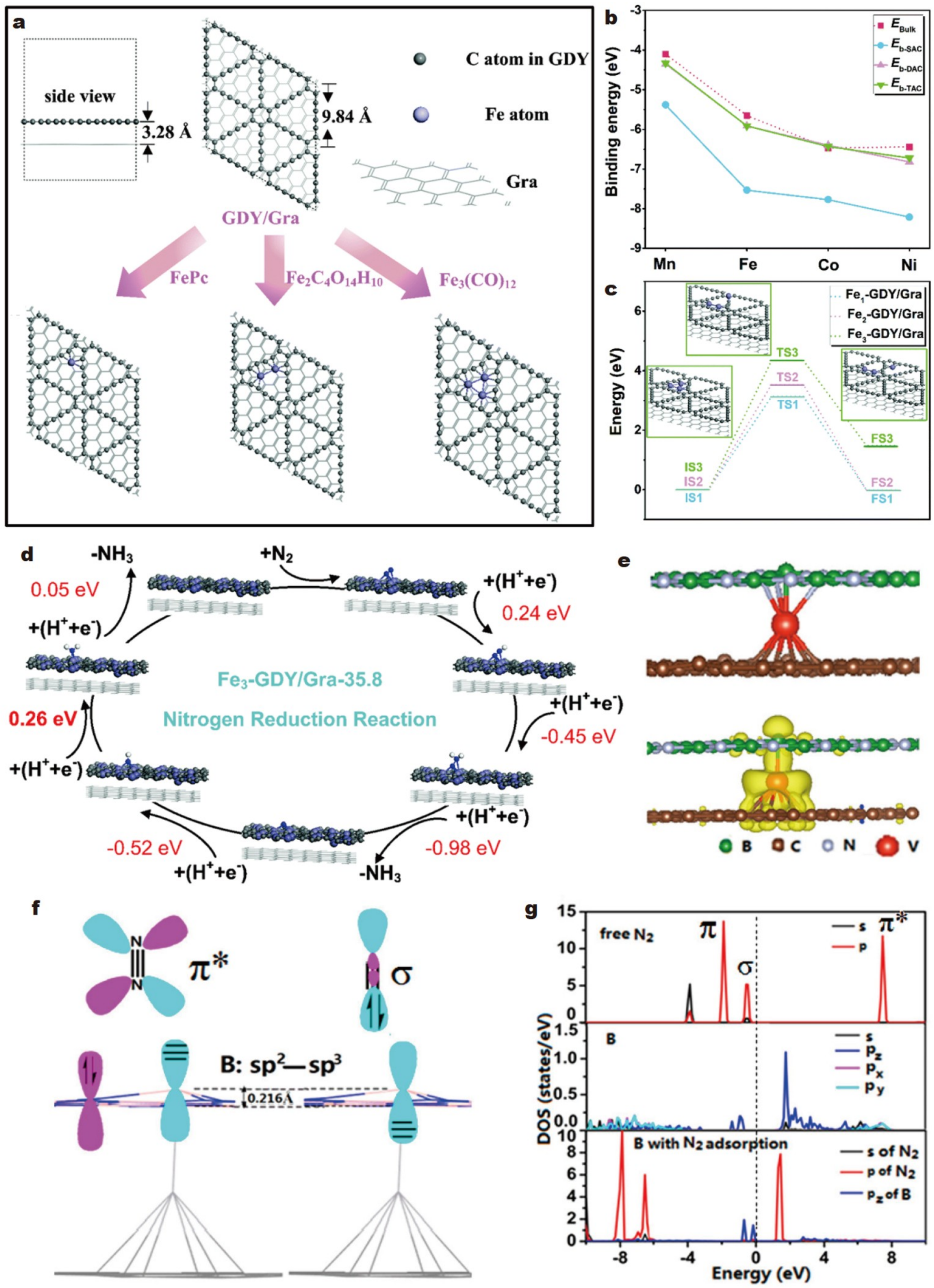

Figure 4 (a) Structural illustration of Fe_x-GDY/Gra along with the corresponding synthetic strategy. (b) Binding energies of M_x-GDY/Gra (M = Mn, Fe, Co, and Ni) and their corresponding cohesive energies in the bulk state. (c) Diffusion paths of a single Fe atom to the nearby pore of GDY/Gra. (d) Free energy profiles for the NRR on Fe_3-GDY/Gra with a mass loading of 35.8 wt%. Reprinted with permission from Ref. [70]. Copyright 2020, The Royal Society of Chemistry. (e) Geometrical structures and partial charge densities of BN/V/G. (f) Schematic illustration of the electron "acceptance-donation" mechanism between the orbitals of N_2 and B. (g) PDOSs of B and N_2 before and after N_2 adsorption. Reprinted with permission from Ref. [78]. Copyright 2020, American Chemical Society.

PPy coating is conducive to N_2 activation on S-Fe_2O_3@PPy. In this case, the potential limiting step (PLS, which is another expression for the PDS) of the NRR on S-Fe_2O_3@PPy is the last step, while the PLSs on Fe_2O_3 and S-Fe_2O_3 are the first step (Fig. 6g). DFT calculations revealed that S-Fe_2O_3@PPy achieves a low U_L of −0.45 V and an NH_3 yield of 22.1 μg h^{-1} mg_{cat}^{-1} with a FE of 24.6%.

Considering the great exploration space of the potential single-atom catalysts (SACs) for the NRR, machine learning (ML) provides a solution to accelerate the discovery of highly efficient catalysts. Zafari *et al.* [86] used a deep neural network (DNN) to predict the NRR performance among B-doped graphene SACs. The ML dataset contained 182 candidate catalysts of B-Gr-SAC, which were constructed by combining seven different types of coordination in SACs and 26 TMs (Fig. 7a). The DNN model (Fig. 7b) was trained in terms of ΔE_{N_2}, $\Delta G_{N_2-N_2H}$ and

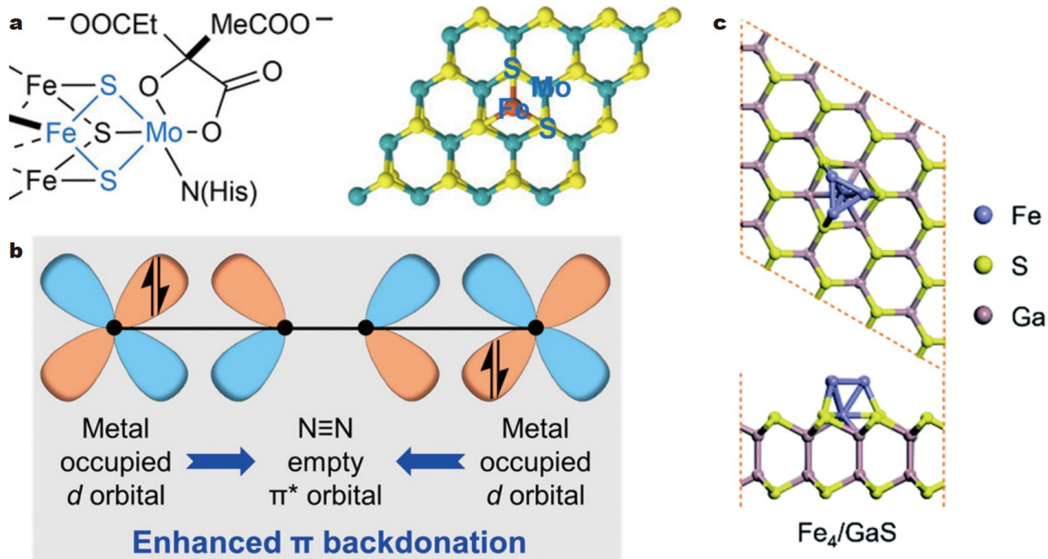

Figure 5 (a) Representation of the nitrogenase FeMo cofactor and optimized structure of Fe deposited on a MoS_2 2D sheet. Reprinted with permission from Ref. [80]. Copyright 2017, Wiley-VCH. (b) Enhanced "donation" mechanism for N_2 activation by double atoms. Reprinted with permission from Ref. [52]. Copyright 2022, American Chemical Society. (c) Structural illustrations of Fe_4/GaS. Reprinted with permission from Ref. [58]. Copyright 2014, The Royal Society of Chemistry.

$\Delta G_{NH_2-NH_3}$, which represent the adsorption energy of N_2 without a free energy correction and the reaction free energies of the first step and the last step. The output of the ML model was the probability of an efficient catalyst, where a high accuracy of a root-mean-square error of 0.11 was achieved with the Light Gradient Boosting Machine (LGBM) model (Fig. 7c). After screening, the optimal catalyst of CrB_3C_1 was obtained, which had a low U_L of −0.29 V *vs.* RHE (Fig. 7d). Chen *et al.* [87] developed ML models based on the boosted regression tree ensemble method to predict the NRR performance among 126 SACs, which were built from nine 2D substrates and 14 TMs. Three ML models were established for evaluating the outputs of ΔG_{PLS}, ΔG_{H*} and $\Delta E_{b\text{-}M}$, which were used to describe the NRR activity, HER activity and stability of the catalysts, respectively. The predicted results of all three models coincide well with the DFT-computed results (Fig. 7e), indicating the satisfactory accuracy of the developed ML models. Moreover, the ML models also exhibit generalizability since the predicted overpotential (η), which is a direct indicator of the NRR activity in experiments, well matches those obtained in previous studies (Fig. 7f). The authors also analyzed the importance of the features of the ML models. Interestingly, the NRR activity (Fig. 7g) is mostly determined by the number of electrons in the doped TMs, while the HER activity (Fig. 7h) is influenced by the Fermi energy of the substrate and the electronegativity and electron affinity of the doped TMs. The above findings obtained from ML models are very helpful for designing SACs with high NRR activity but low HER activity. Overall, by regulating the interactions between active sites and substrates, the NRR activity can be greatly promoted.

Regulating the electronic structures of the active sites

The targets of regulating the electronic structures of active sites include enhancing the "acceptance-donation" mechanism and optimizing the interactions between substrates and active atoms [88]. As is known, highly efficient N_2 activation requires not only the synergy of the occupied and empty orbitals of the active sites but also favorable orbital matching in both the energies and spatial orientations. Therefore, a comprehensive understanding of the electronic orbitals, especially the suborbitals, should be established before material design. In this section, the electronic regulation strategies for the active sites are summarized into three modes: nonmetal to metal, metal to metal, and nonmetal only.

Mode 1 is the most common mode in which the d orbitals of TMs can be effectively modulated by covalent bonding to nonmetal atoms. In recent years, successful explorations of nitrides, oxides, carbides, sulfides, and borides for the NRR have been conducted using DFT calculations. For TMNs, Kong *et al.* [89] theoretically investigated the NRR performance on the (001) and (110) facets of Mo_5N_6 (Fig. 8a). The Mo-terminated surfaces have lower surface energies than the N-terminated surfaces; thus, the former is mainly exposed. The NRR on Mo-terminated Mo_5N_6(001) and Mo_5N_6(110) follows the enzymatic mechanism, and the free energy diagrams are shown in Fig. 8b, c, respectively. The PDS of the NRR on Mo_5N_6(001) is the NH_2^* to NH_3^* step, with ΔG = 0.52 eV, and that on Mo_5N_6(110) is the $NHNH^*$ to $NHNH_2^*$ step, with ΔG = 0.46 eV. The distinct NRR performances can be attributed to different coordination numbers for surface N atoms. Jin *et al.* [90] developed a W_2N_3 nanosheet for the NRR and demonstrated that N vacancies are active sites. The charge density difference diagram in Fig. 8d illustrates that the N vacancies produce an electron-deficient area on the surface, which act as N_2 activation sites due to an enhanced "acceptance" mechanism. The ΔG for the first NRR step is thus only 0.55 eV (Fig. 8e). Experimentally, W_2N_3 shows an NH_3 yield of 11.66 ± 0.98 μg h^{-1} mg_{cat}^{-1} and a FE of 11.67% ± 0.93%.

TMOs are promising substrates and can also be used solely as NRR catalysts by imposing lattice strain or producing O vacancies. Li *et al.* [91] discovered that a strain effect on TiO_2 could improve its NRR performance. The charge density difference of N_2 adsorbed on strained TiO_2 shows that electrons

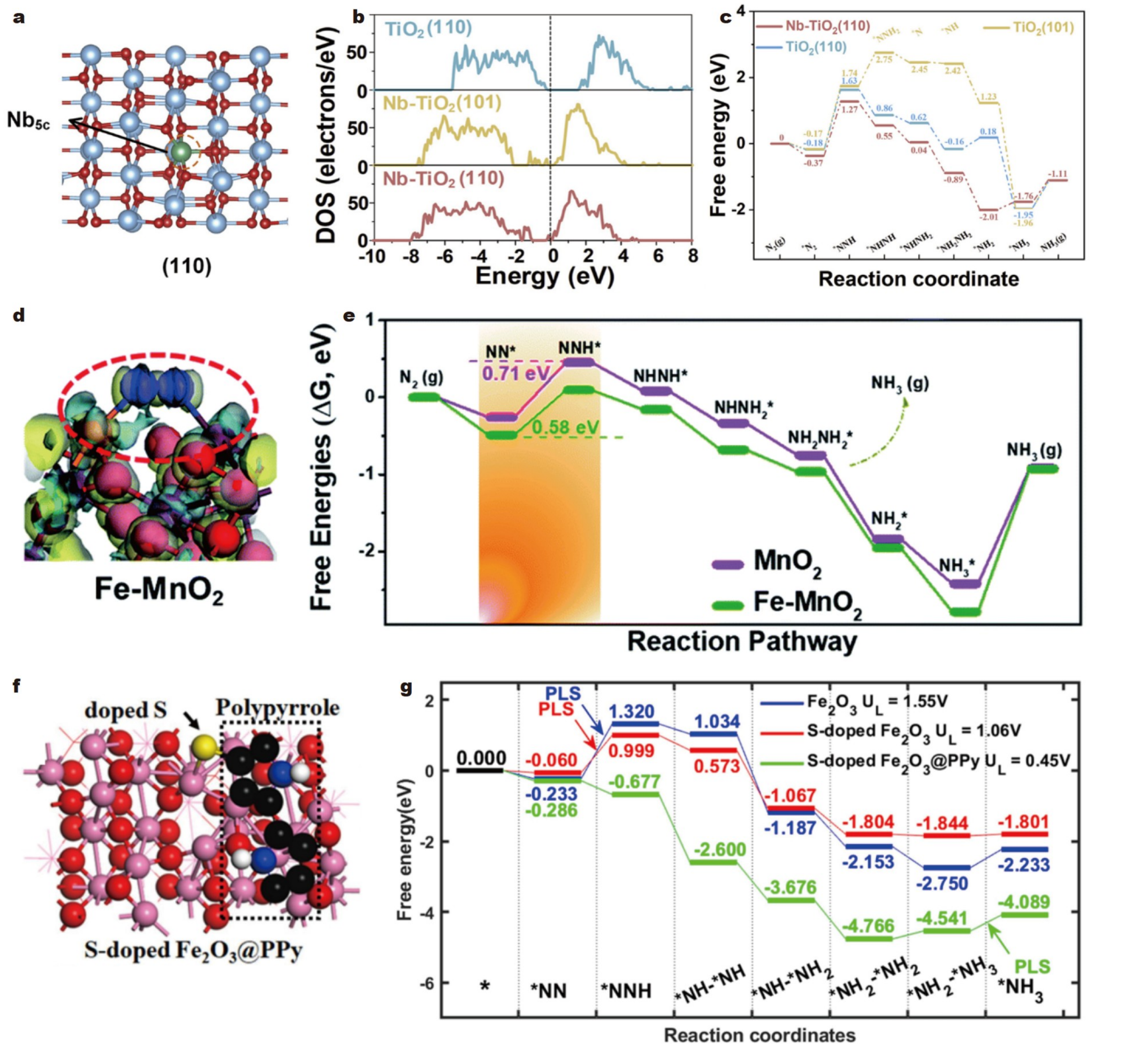

Figure 6 (a) Structural illustration of Nb-TiO_2(110). (b) PDOSs of TiO_2(110), Nb-TiO_2(101), and Nb-TiO_2(110). (c) Gibbs free energy diagram for the NRR on TiO_2(110), Nb-TiO_2(101), and Nb-TiO_2(110). Reprinted with permission from Ref. [83]. Copyright 2022, Elsevier. (d) Charge density difference of N_2 adsorbed on Fe-MnO_2(211). (e) Gibbs free energy diagram for the NRR on MnO_2(211) and Fe-MnO_2(211). Reprinted with permission from Ref. [84]. Copyright 2022, The Royal Society of Chemistry. (f) Top view of a structural illustration of S-Fe_2O_3@PPy. (g) Gibbs free energy diagram for the NRR on Fe_2O_3, S-Fe_2O_3 and S-Fe_2O_3@PPy. Reprinted with permission from Ref. [85]. Copyright 2023, Elsevier.

mainly accumulate on N atoms and are depleted between them (Fig. 8f), suggesting effective N_2 activation. Compared with that on pristine TiO_2, the ΔG of the PDS of the NRR on strained TiO_2 decreases from 0.73 to 0.61 eV (Fig. 8g). As a result, an NH_3 yield of 16.67 μg h^{-1} mg_{cat}^{-1} and a FE of 26% are obtained by strained TiO_2 in experiments. Zhang *et al.* [92] developed Nb-based MXenes with O vacancies for the NRR (Fig. 8h). The O vacancies serve as adsorption sites for N_2 with an end-on configuration. The NRR proceeds *via* the distal mechanism, and the PDS is the first step, with a ΔG of 0.86 eV (Fig. 8i). The results show an NH_3 yield of 29.1 μg h^{-1} mg_{cat}^{-1} and a FE of 11.5%. Xia *et al.* [93] proposed that ZrO_2 with an O vacancy favors N_2 adsorption and activation. The N≡N bond length increases from 1.114 to 1.200 Å when N_2 is adsorbed on Zr sites in a side-on configuration, which facilitates the N_2 reaction. Experimentally, the large concentration of oxygen defects in ZrO_2 allows for a yield of 9.63 μg h^{-1} mg_{cat}^{-1} and a FE of 12.1%.

TMCs with 2D MXene structures have been widely explored as catalysts in recent years since their large specific surface areas can provide abundant active sites. Wang *et al.* [94] systematically explored a series of M_2C (M = Sc, Ti, V, Cr, Mn, Fe, Zr, Nb, Mo, Ta and Hf) MXenes for the NRR. The M_2C MXenes provide multiple active sites for the NRR, where N_2 can adsorb on both the top and hollow sites (Fig. 9a). A volcano plot is plotted in Fig. 9b, which describes the relation between the adsorption energy of N_2 and the NRR performance. The Fe_2C MXenes are located nearest to the top of the volcano and achieve a remarkable computed U_L of −0.23 V. In addition, MXenes can be used as substrates for SACs. Huang *et al.* [95] proposed that Mo-doped Mo_2CO_2 MXene is a potential candidate for the NRR.

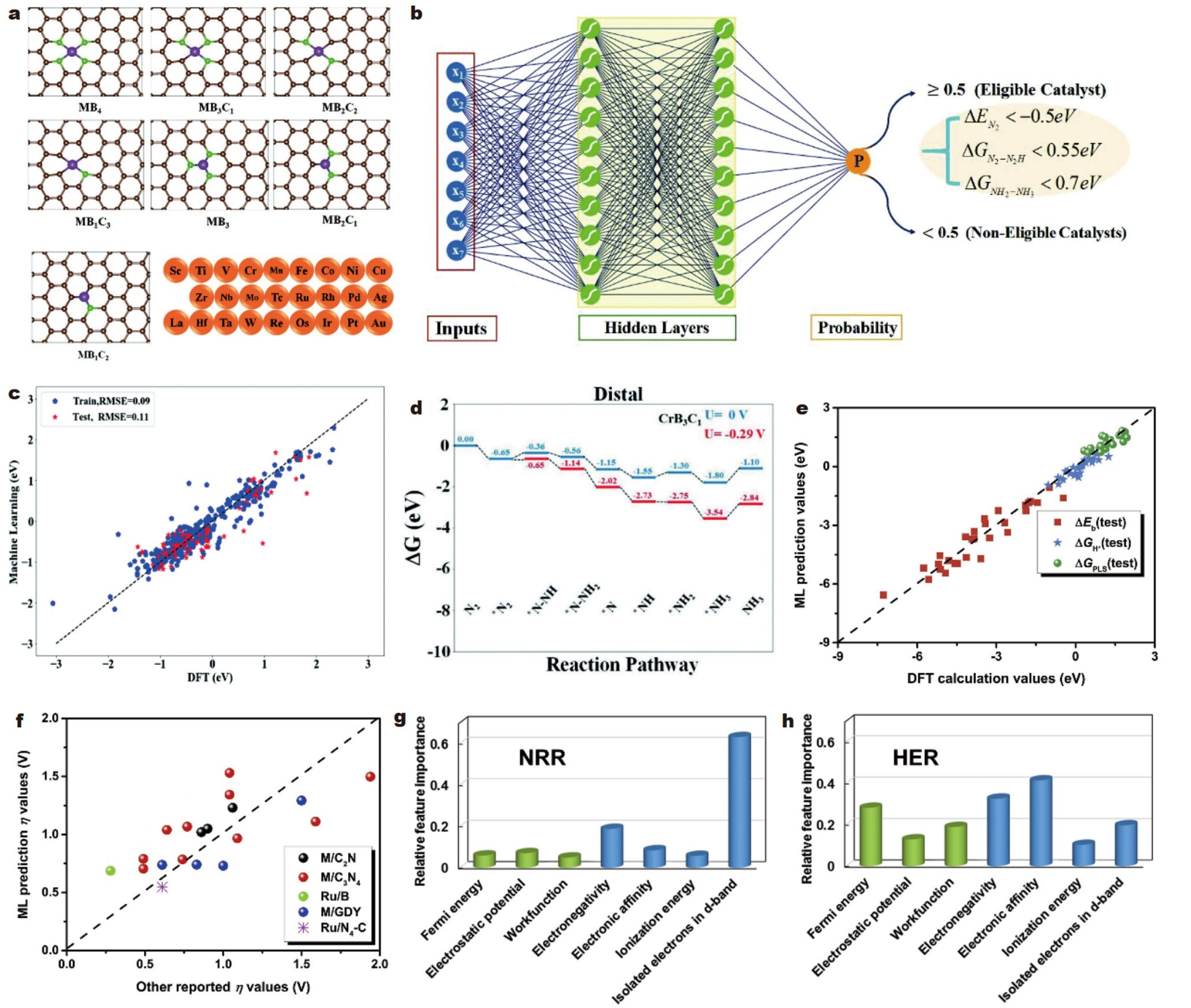

Figure 7 (a) Structures of B-doped graphene SACs with the TMs considered for screening. (b) Artificial neural network architecture with ten neurons in each hidden layer. (c) Parity plot comparing the DFT-calculated and ML-predicted outputs for the NRR performance. (d) Gibbs free energy diagram for the NRR on CrB_3C *via* the distal mechanism. Reprinted with permission from Ref. [86]. Copyright 2020, The Royal Society of Chemistry. (e) Parity plot comparing the DFT-calculated and ML-predicted outputs for ΔE_b, ΔG_{H*} and ΔG_{PLS}. (f) Comparisons between ML-predicted overpotential (η) and literature η values. (g) Feature importance in the ML model for ΔG_{PLS}. (h) Feature importance in the ML model for ΔG_{H*}. Reprinted with permission from Ref. [87]. Copyright 2021, Elsevier.

The PDS of the NRR on $Mo@Mo_2CO_2$ is the first step, with $\Delta G = -0.32$ V (Fig. 9c, d).

Transition metal sulfides (TMSs) show remarkable NRR performance since S plays an important role in natural nitrogenase. Liu *et al*. [96] developed a metallic 1T phase of MoS_2 for the NRR. 1T-MoS_2 exhibits stronger N_2 adsorption than 2H-MoS_2; thus, it greatly facilitates the NRR process. It achieves a high NH_3 yield of 71.07 μg h^{-1} mg_{cat}^{-1} and a FE of 21.01%. Yin and Du [97] imposed surface defects on the 2D Fe monochalcogenides FeX (X = S, Se), which enhanced the N_2 activation. According to DFT calculations, the first step is very facile on FeS-V_s and FeSe-V_{Se} (Fig. 9e–g). The PDS is the third step for FeS-V_s, with $\Delta G = 0.65$ eV, and is the last step for FeS-V_s, with $\Delta G = 0.84$ eV.

Transition metal borides (TMBs) are also attracting interest for the NRR. Mo is the main investigated TM for the NRR due to its nearly optimal electronic structure for N_2 activation, as well as its close proximity to the top of the volcano plots describing the NRR activities [40,98]. Our group proposed that the electrons in the d_{z^2} orbitals of Mo atoms can be transferred to B atoms by bonding; thus, MoB_2 was proposed for the NRR [41]. As shown in Fig. 10a, the geometry of MoB_2 has an alternating layered structure of Mo atoms and B atoms, and the electronic structure of the Mo atoms on the surface has been modified to satisfy the "acceptance" mechanism. The N_2 activation nature on MoB_2 is elucidated by the PDOS in Fig. 10b, where the bonding states (in the range from −5 to −7 eV) indicate that the Mo-d orbitals accept the lone-pair electrons of N_2, and the bonding states (in the range from −3 to 0 eV) reflect the electrons filling in the π* orbitals of N_2. As a result, activation of the N≡N bond is promoted on MoB_2. In particular, the simulation results of the high NRR activity of MoB_2 were ver-

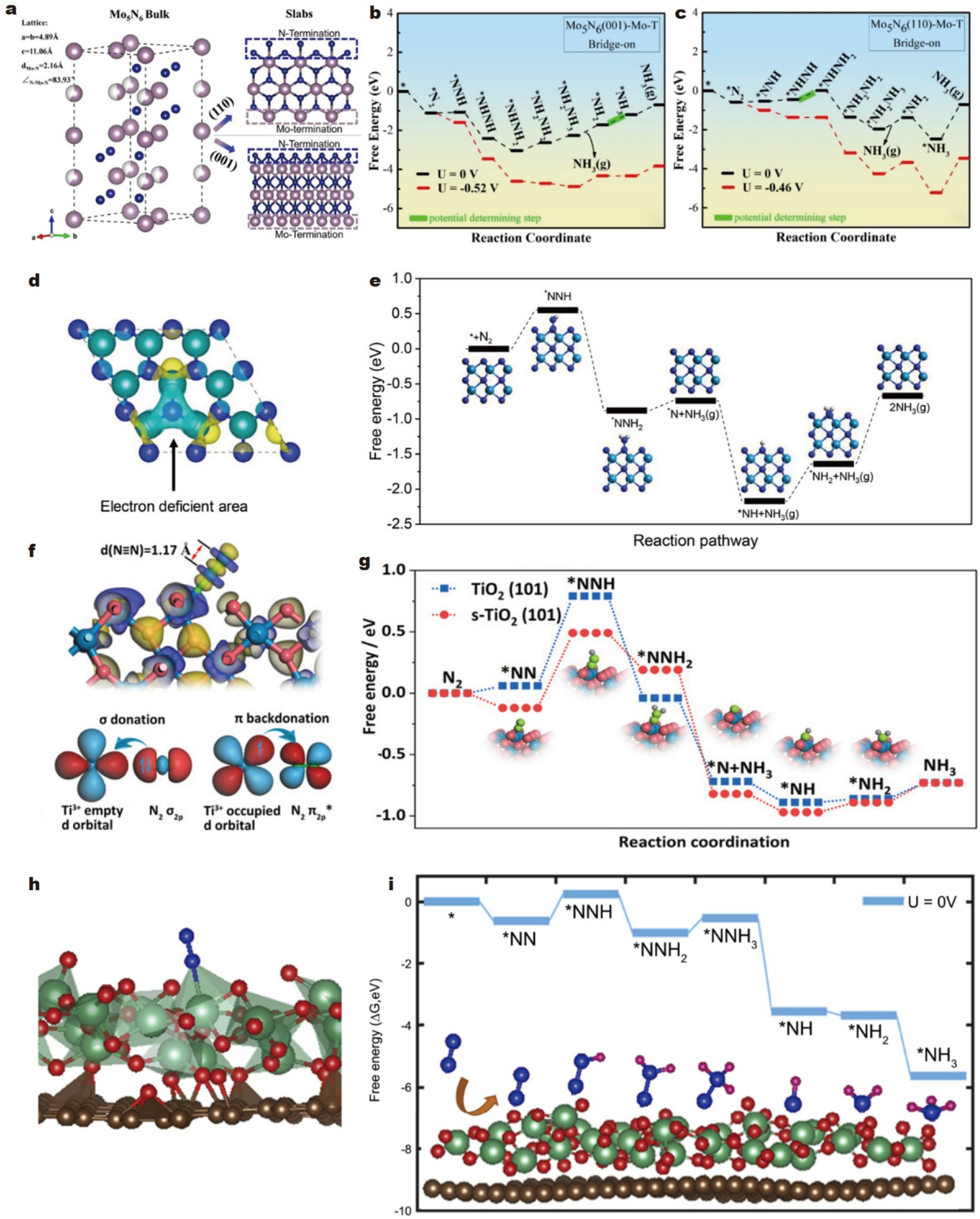

Figure 8 (a) Geometric structures of bulk Mo_5N_6 and supercells of the (001) and (110) facets. (b) Gibbs free energy diagram for the NRR on Mo-terminated Mo_5N_6(001). (c) Gibbs free energy diagram for the NRR on Mo-terminated Mo_5N_6(110). Reprinted with permission from Ref. [89]. Copyright 2021, Wiley-VCH. (d) Charge density difference diagram of N vacancies on W_2N_3. (e) Gibbs free energy diagram for the NRR on NV-W_2N_3 along with the corresponding configurations of all intermediates. Reprinted with permission from Ref. [90]. Copyright 2019, Wiley-VCH. (f) Charge density difference diagram of N_2 adsorbed on the strained TiO_2, and illustrations of the N_2 activation mechanism. (g) Gibbs free energy diagram for the NRR on TiO_2 and the strained TiO_2 along with the corresponding intermediate configurations. Reprinted with permission from Ref. [91]. Copyright 2020, Wiley-VCH. (h) Structural illustrations of the N_2-adsorbed Nb_2O_5/C (green: Nb; red: O; blue: N). (i) Gibbs free energy diagram for the NRR on Nb_2O_5/C along with the surface configurations of intermediates. Reprinted with permission from Ref. [92]. Copyright 2023, Elsevier.

ified by a proof-of-concept experiment, where MoB_2 exhibited excellent NRR performance with an NH_3 yield rate of 40.94 μg h^{-1} mg_{cat}^{-1} and a FE of 30.84% at −0.4 V *vs*. RHE. Interestingly, Feng *et al*. [99] demonstrated that the B vacancies on NbB_2 nanoflakes (NFs) play an important role in N_2 activation. This catalyst has an NH_3 yield rate of 30.5 μg h^{-1} mg_{cat}^{-1} at −0.4 V *vs*. RHE and a superhigh FE of 40.2%.

In mode 2, since the electronic modulation is based on

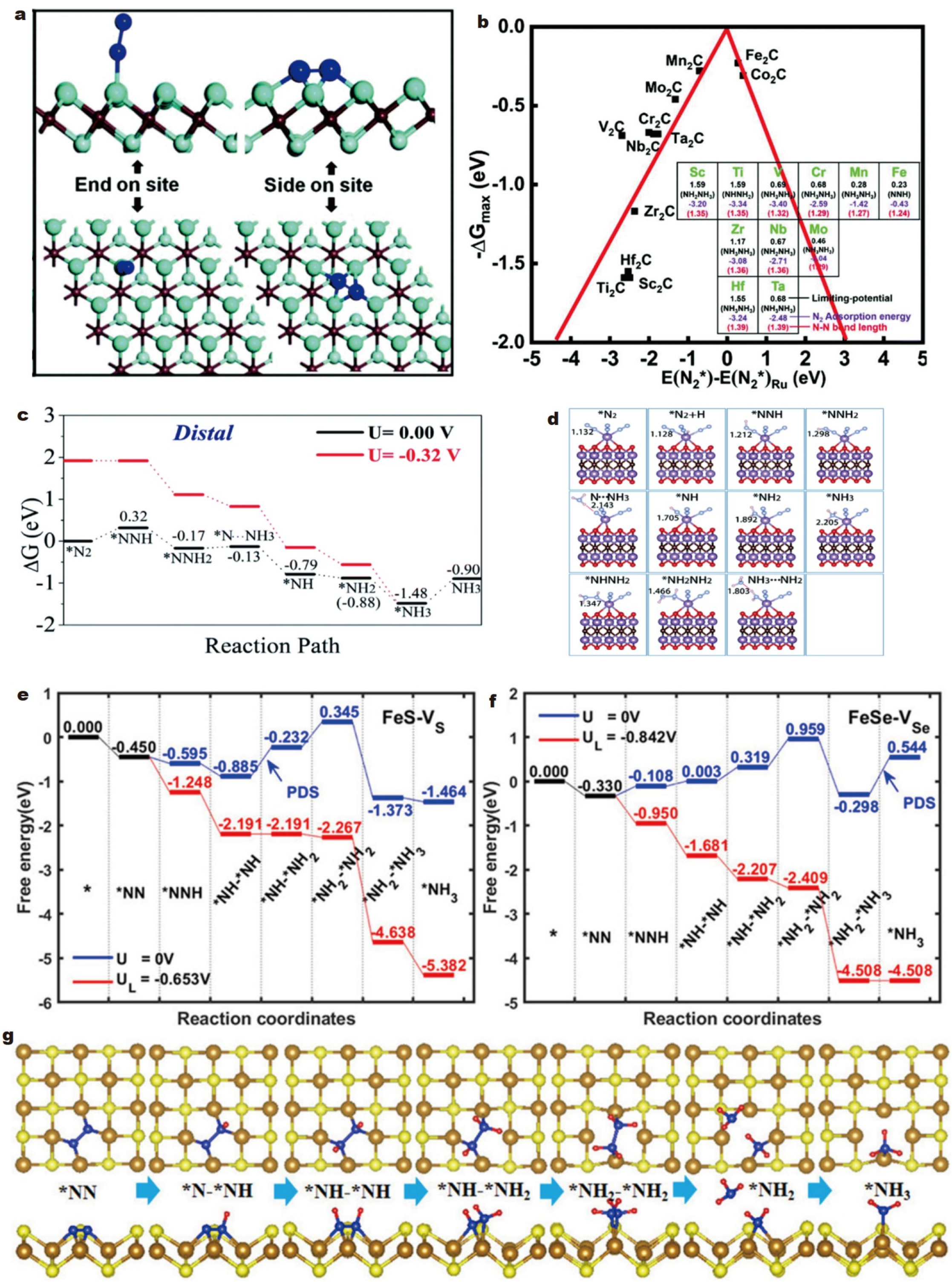

Figure 9 (a) Geometric structures for N_2 adsorption on the top and hollow sites of M_2C MXenes. (b) Volcano diagram of the NRR activity for all M_2C catalysts. Reprinted with permission from Ref. [94]. Copyright 2020, The Royal Society of Chemistry. (c) Gibbs free energy diagram for the NRR on $Mo@Mo_2CO_2$ along with (d) the corresponding configurations of all intermediates. Reprinted with permission from Ref. [95]. Copyright 2019, The Royal Society of Chemistry. Gibbs free energy diagram for the NRR on (e) FeS-V_S and (f) FeSe-V_{Se}, along with (g) the corresponding configurations of all intermediates. Reprinted with permission from Ref. [97]. Copyright 2022, Wiley-VCH.

metallic bonding, the effect is normally weaker than that in mode 1, which is based on covalent bonding. Pure metal nanostructures show improved NRR performance compared with bulk metals due to the decrease in the coordination numbers of the active sites. Bao *et al.* [100] demonstrated that tetrahexahedral Au nanorods enclosed by stepped facets could be used to catalyze the NRR at room temperature and atmospheric pressure. The catalysts resulted in a high NH_3 yield of

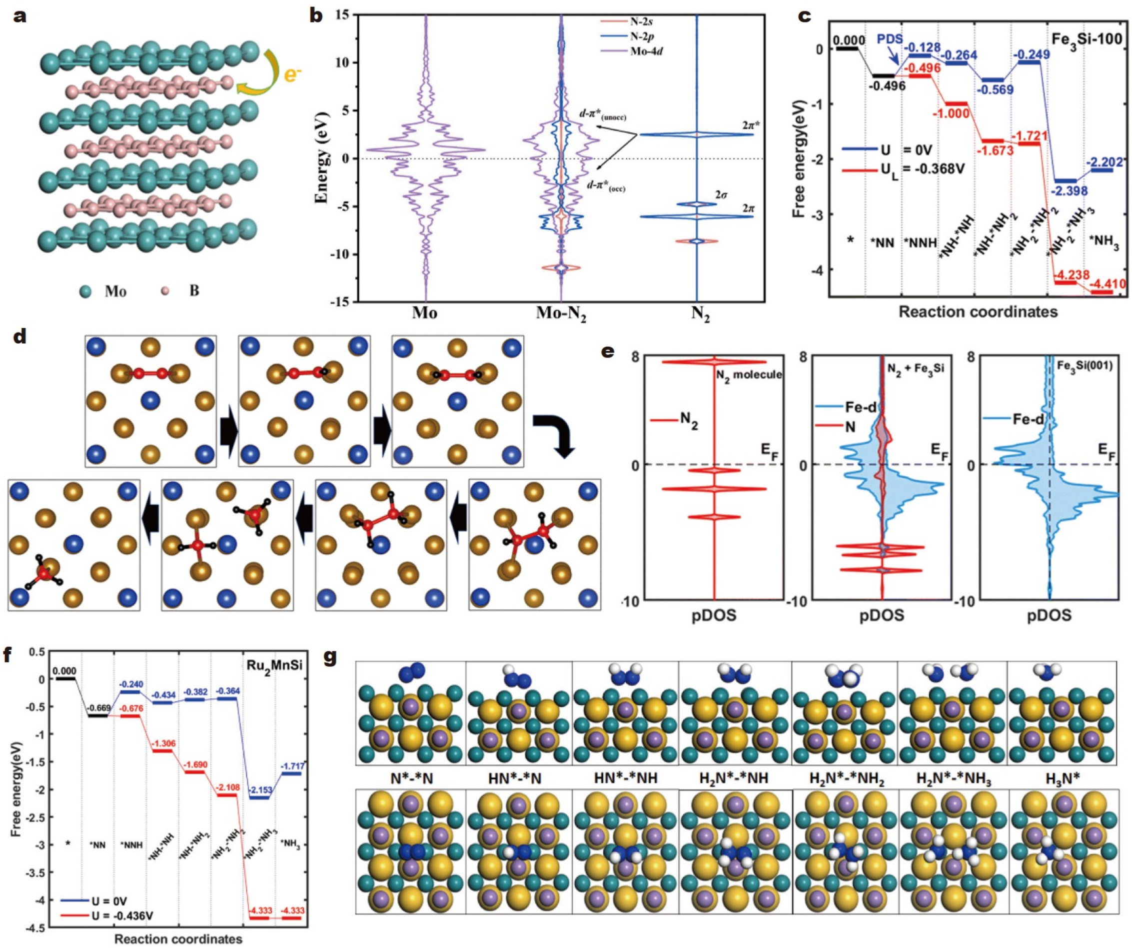

Figure 10 (a) Geometric structures of MoB_2. (b) PDOS of N_2 on the Mo atoms of MoB_2. Reprinted with permission from Ref. [41]. Copyright 2021, Elsevier. (c) Gibbs free energy diagram for the NRR on Fe_3Si along with (d) the corresponding configurations of intermediates. (e) PDOSs of free N_2, N_2 adsorbed on Fe_3Si, and individual Fe_3Si. Reprinted with permission from Ref. [103]. Copyright 2023, The Royal Society of Chemistry. (f) Gibbs free energy diagram for the NRR on Ru_2MnSi along with (g) the corresponding configurations of intermediates. Reprinted with permission from Ref. [104]. Copyright 2022, American Chemical Society.

1.648 μg h^{-1} cm^{-1}. Wang *et al.* [101] reported carbon black-supported Pd nanoparticles (Pd/C) that strongly promoted the hydrogenation of N_2. The Pd/C catalyst exhibited an NH_3 yield of 4.5 μg h^{-1} mg_{cat}^{-1} and a FE of 8.2% at 0.1 V *vs.* RHE.

Alloying can be used to establish multiple active sites for the NRR to overcome the limitation of the scaling relations between the adsorption energies of NNH^* and NH_2^* on a single active site. Our group has proposed intermetallic Ni_3Mo for the NRR and realized the separation of active sites [102]. The first hydrogenation step of NNH^* formation occurs at the Mo–Mo sites, while the last step of NH_2^* to NH_3^* occurs at the Mo–Ni sites. Therefore, Ni_3Mo successfully avoids the scaling relations. Yin *et al.* [103] systematically investigated the NRR performance of a series of bimetallic alloys composed of iron and group-IVA elements (Si, Ge and Sn). Among all the candidates, Fe_3Si has the highest catalytic activity for the NRR, with a low U_L of −0.37 V *vs.* RHE. The PDS of the NRR on Fe_3Si is the first step (Fig. 10c, d), where the intermediates gradually shift during the NRR process, reducing the total reaction-free energy. Interestingly, the PDS of the NRR on Fe_3Ge is the fourth step, while those on $Fe_{13}Ge_3$ and Fe_3Sn are the last step. This suggests that the optimal NRR catalysts should not only induce strong N_2 activation but also balance all six elementary steps. The N_2 activation on Fe_3Si was considered (Fig. 10e), where the large spin polarization of the Fe atom causes significant electron transfer to the π* orbitals of N_2, thus weakening the stable N≡N bond. Furthermore, Yin and Du [104] also examined the NRR performance on a ternary Ru_2MnSi alloy. Owing to the diversity of active sites on the catalyst surfaces, both the first and last NRR steps can be promoted, and the ΔG values of these two steps are 0.43 and 0.44 eV (Fig. 10f, g), respectively. Interestingly, a novel electronic modulation mechanism was found based on the metallic interactions in mode 2. Single-atom alloy catalysts, with weak interactions between the doped atoms and the substrate matrix, can form special electronic states resembling those of a free atom [105,106]. During N_2 adsorption, electronic redistribution of the d-states of the TMs is induced by the stronger TM-N interaction to satisfy the needs of the "acceptance-donation" mechanism, i.e., the coexistence of empty and occupied orbitals [107,108]. Thus, N_2 activation can be enhanced.

In mode 3, metal-free catalysts are developed for the NRR due to their much weaker binding energies to protons than those of metal-based catalysts. B has played an important role since its electronic configuration ($2s^22p^1$) satisfies the requirements of the "acceptance-donation" mechanism [109]. Liu *et al.* [110] constructed 21 B-based SACs for the NRR (Fig. 11a) to understand the electronic modulation mechanism arising from substrates where B serves as the active site. They established a NRR volcano plot through a thorough computation of the NRR activity (Fig. 11b). B-doped graphene is closest to the top of the volcano plot and has a high NRR activity, with a U_L of −0.31 V *vs.* RHE. In particular, Li *et al.* [111] proposed a carbon-decorated graphitic carbon nitride ($C/g\text{-}C_3N_4$) for the NRR (Fig. 11c). The catalytic centers of $C/g\text{-}C_3N_4$ are akin to those of high-efficiency "N-heterocyclic carbenes", where the doped C atoms possess both lone-pair electrons and partially occupied p_z orbitals. These features satisfy the requirements of the "acceptance-donation" mechanism. The electronic structures of N_2 on $C/g\text{-}C_3N_4$ are plotted in terms of the charge density difference and PDOS in Fig. 11d, e. There is obvious orbital hybridization between the 2p orbitals of N_2 and the 2p orbitals of C atoms, implying that N_2 has been activated. By following the enzymatic pathway (Fig. 11f), NRR activity with U_L = −0.21 V *vs.* RHE is realized. Notably, although the ΔG_d of NH_3 is as high as 2.31 eV, the energy released in the NRR process of 3.28 eV can completely provide the energy needed for NH_3 desorption. Additionally, recent studies have proposed that NH_3 desorption indirectly occurs *via* further protonation to NH_4^+ under acidic or alkaline conditions, and that the formed NH_4^+ can be readily soluble in electrolytes [75,112]. Thus, NH_3 desorption may not be a problematic obstacle in the NRR.

Developing a new reaction mechanism

In the associative mechanism, both the first hydrogenation step of N_2^* to NNH^* and the last hydrogenation step of NH_2^* to NH_2^* could have difficulty proceeding [113]. Hence, a smart strategy is to circumvent these steps by developing a new mechanism. The MvK mechanism has been proposed on TMNs and TMCs, in which the N atoms on the lattice are reduced to NH_3 and then replenished by N_2 molecules (Fig. 12a) [114]. Ellingsson *et al.* [46] performed systematic DFT calculations to evaluate the NRR performance on TMCs. The representative structure of WC for the (100) facet of the rocksalt (RS) structure is shown in Fig. 12b. The N_2 molecule can readily undergo dissociative adsorption on the C vacancy on the surface. The entire reaction pathway on WC is illustrated in Fig. 12c. The lattice N atom is hydrogenated to the final NH_3 step by step, where the ΔG of the PDS is only 0.35 eV, indicating the high NRR activity.

Noble metal catalysts with high NRR activity have been reported, but the general reaction mechanism cannot fully explain this activity due to their relatively weak interactions with N_2 [100]. Therefore, a surface hydrogenation mechanism on noble metal catalysts (Fig. 12d) was proposed by Wang's group [48]. Namely, the Volmer reaction for H adsorption first occurs on the catalyst surface, in which the N_2 molecule can directly react with two adsorbed H^* to form the $N_2H_2^*$ species. In the latter steps, the $N_2H_2^*$ intermediates can be spontaneously reduced to NH_3. The first step of H adsorption was identified as the PDS for the entire process, which accounted for the low electrode potential required for the NRR to proceed. This work not only bridged the gap between the experimental results and theoretical understandings but also stimulated more interests in developing new catalytic mechanisms for high-efficiency NRR.

It has been proposed that the HER can be kinetically sup-

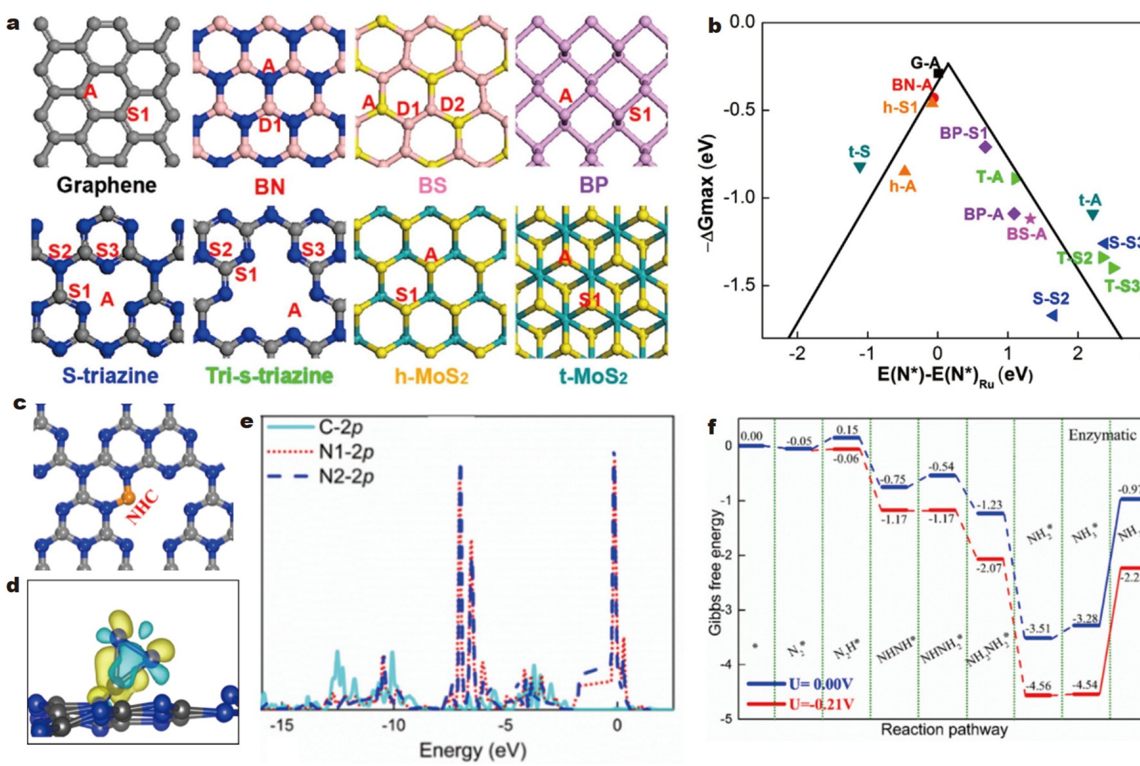

Figure 11 (a) Structural illustrations of the 2D materials proposed as the substrates for boron atoms. The black, blue, rose, yellow, purple, and cyan spheres represent C, N, B, S, P, and Mo, respectively. (b) Volcano diagrams for the B-doped 2D materials for the NRR. Reprinted with permission from Ref. [110]. Copyright 2019, American Chemical Society. (c) Structural illustration of $C/g\text{-}C_3N_4$. (d) Charge density difference and (e) PDOS of N adsorbed onto $C/g\text{-}C_3N_4$ in a side-on configuration. (f) Free energy profiles of the NRR on $C/g\text{-}C_3N_4$ along the enzymatic pathway. Reprinted with permission from Ref. [111]. Copyright 2019, Elsevier.

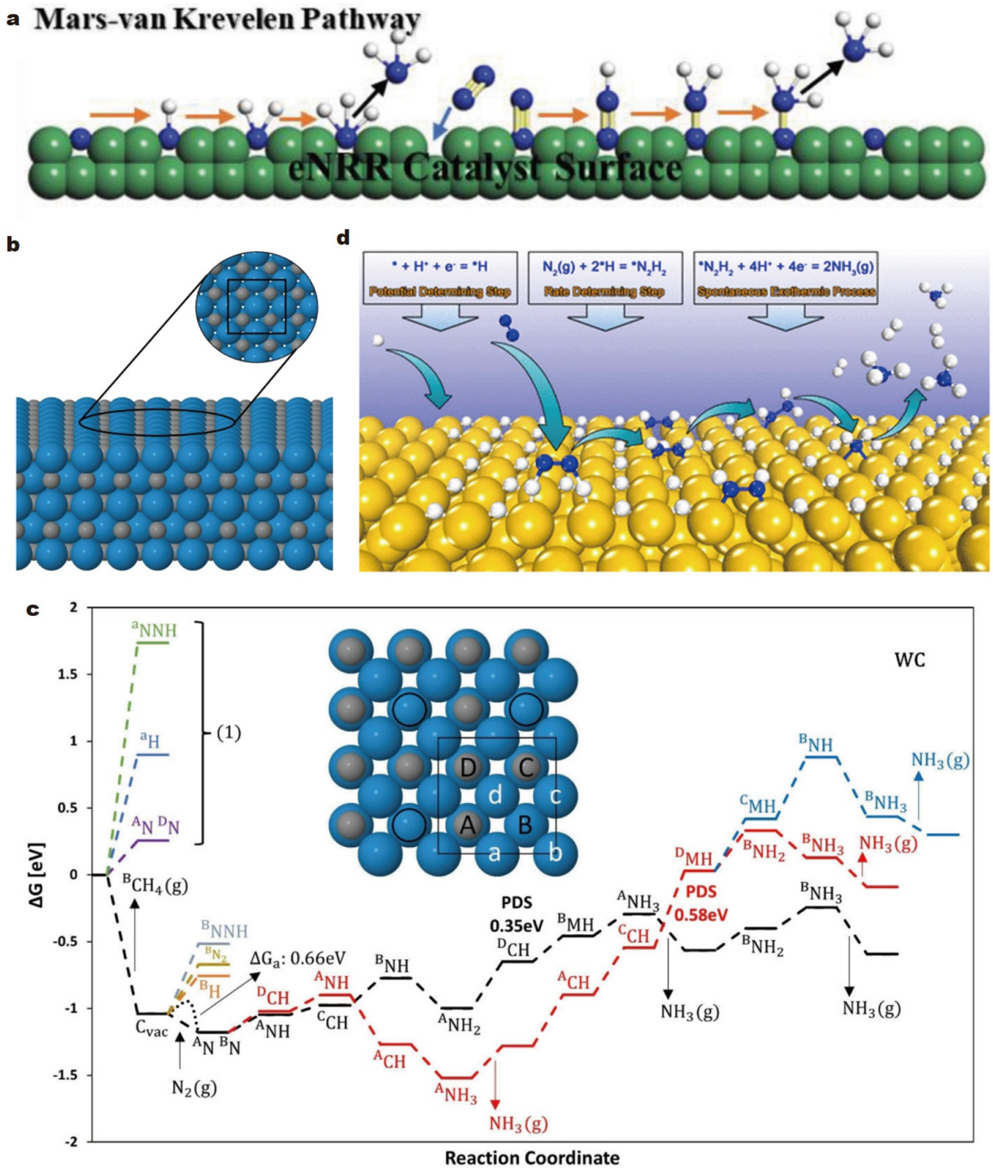

Figure 12 (a) Schematic illustration of the MvK pathway for the NRR. Reprinted with permission from Ref. [114]. Copyright 2020, Wiley-VCH. (b) Structural illustration of WC for the (100) surface of the rocksalt structure. (c) Free energy diagram of the NRR following the MvK pathway on WC. Reprinted with permission from Ref. [46]. Copyright 2023, Wiley-VCH. (d) Schematic of the surface hydrogenation mechanism for the NRR on noble-metal-based catalysts. Reprinted with permission from Ref. [48]. Copyright 2019, American Chemical Society.

pressed under alkaline conditions, but the slow dynamics of H^+ transfer can also limit the reaction rate of the NRR [115]. Our group [116] proposed a hydrogen spillover mechanism under alkaline conditions for the NRR, in which the H atoms in adsorbed OH^* species serve as H sources and thus improve the kinetics of the NRR. Following this strategy, a catalyst of Fe-doped Mo_2N with a vacancy (Fe/SV-Mo_2N) was developed, whose structure is shown in Fig. 13a. The vacancy of Fe/SV-Mo_2N can spontaneously adsorb three OH^- ions, resulting in H spillover from OH^* to N_2^*. The entire reaction pathway with H spillover is shown in Fig. 13b, where all the hydrogenation steps are spontaneous except for the NH_2NH^* to $NH_2NH_2^*$ step. The ΔG of this step is only 0.22 eV, corresponding to a very facile NRR process with the assistance of H spillover under alkaline conditions. A proof-of-concept experiment was further performed to confirm the superior electrocatalytic activity of Fe/SV-Mo_2N. The NH_3 yield rate is 36.4 μg h^{-1} mg_{cat}^{-1}, which is higher than that of intact Mo_2N. Lv *et al.* [117] proposed an analogous reaction mechanism on an MXene catalyst with hydroxyl termination. As shown in Fig. 13c, N_2 is hydrogenated by the surface H atoms in the OH terminal group, and the remaining H vacancies can easily self-repair. By following this mechanism, the OH-terminated MXenes exhibit higher NRR activity than the bare MXenes (Fig. 13d).

The above strategies are akin to the associative mechanism, in which N_2 is first hydrogenated rather than the N≡N bond broken. A dual-site dissociative mechanism was proposed by Abild-Pedersen's group [118]: N_2 is first dissociated by confined dual sites, and the separate N atoms are reduced to NH_3 molecules. The energy barrier for N≡N bond breaking is greatly reduced by following the dual-site dissociative mechanism, which can be attributed to the stabilized transition state and the

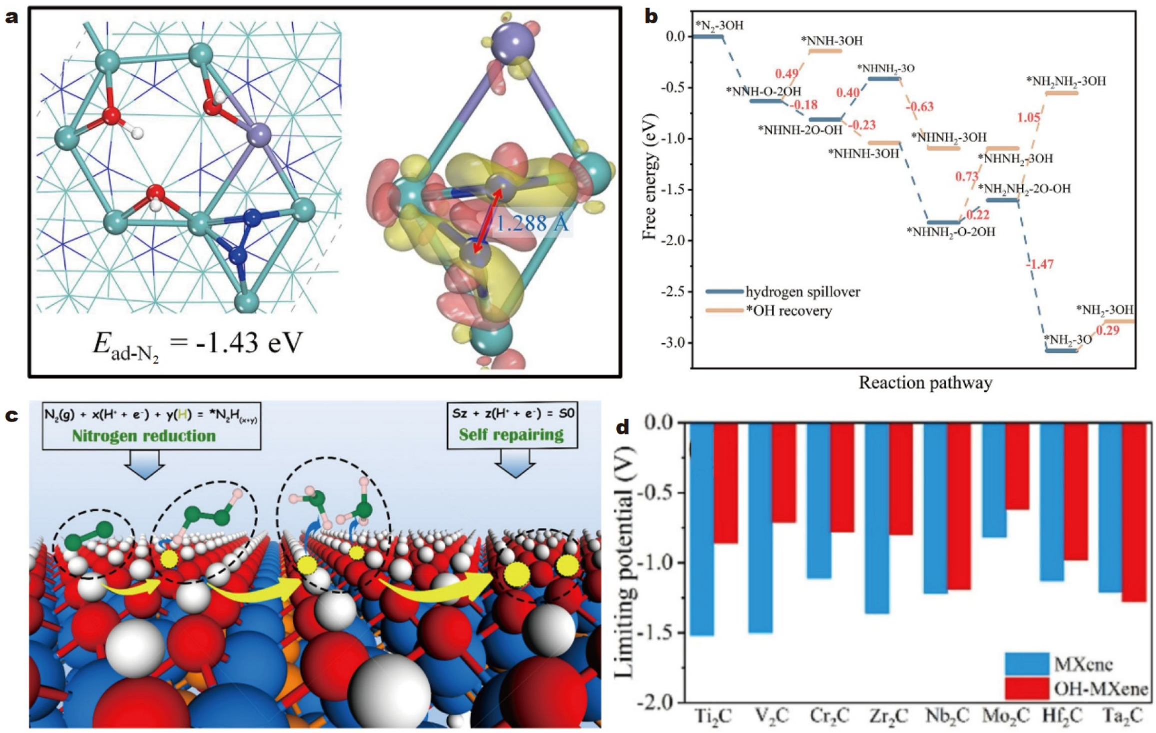

Figure 13 (a) Adsorption configurations of N_2^* on Fe/SV-Mo_2N&3OH* along with the charge density difference, where the yellow and pink isosurfaces indicate electron accumulation and depletion, respectively. (b) Free energy profiles of the NRR with hydrogen spillover and OH* recovery processes. Reprinted with permission from Ref. [116]. Copyright 2023, Elsevier. (c) Schematic of the reaction mechanism for the NRR on $M_2C(OH)_2$. (d) Comparison of the onset potentials between M_2C and $M_2C(OH)_2$. Reprinted with permission from Ref. [117]. Copyright 2021, American Chemical Society.

enhanced "donation" mechanism at the dual sites. Table 1 displays the computational and experimental NRR activities of the catalysts discussed in this review.

STRATEGIES TO IMPROVE THE SELECTIVITY

As mentioned above, the NRR is severely limited by the competitive HER under aqueous solution conditions and, thus, the decrease in the FE [115]. To address the selectivity issue induced by the HER, the reaction mechanisms of the HER should first be understood. Thermodynamically, the HER performance is determined by ΔG_{H^*}, whose ideal value is close to zero [127,128]. Kinetically, the HER involves only two proton-electron transfer steps, and the first step of H^* formation at the active sites, i.e., the Volmer step, is the most important step [129]. In this section, the strategies used to suppress the HER based on thermodynamic and kinetic methods are summarized.

Thermodynamic suppression of the HER

The thermodynamic methods for suppressing the HER include (1) weakening H adsorption and (2) increasing the U_L of the HER. That is, a stronger $\Delta G_{N_2^*}$ than ΔG_{H^*} indicates dominant N_2 adsorption onto the active sites. The active sites for the NRR would, therefore, not be blocked by H^+. A lower $U_{L\text{-NRR}}$ than $U_{L\text{-HER}}$ means that a lower applied potential is required to trigger the NRR than the HER. These thermodynamic parameters can be accurately acquired by DFT calculations. Zhao *et al.* [98] proposed a theoretical estimation of the selectivity for the NRR (f_{NRR}) based on the difference (δG) between $\Delta G_{PDS\text{-HER}}$ and $\Delta G_{PDS\text{-NRR}}$ according to the Boltzmann distribution:

$$f_{NRR} = 1/(1+\exp[-\delta G/k_BT]), \quad (1)$$

where k_B is the Boltzmann constant and T is the temperature. f_{NRR} represents the mole fraction of NH_3 in the total product stream, which assumes that the reaction rates of the NRR and HER are determined only by the thermodynamic reaction energy of their PDS. They designed a NRR catalyst of Mo atoms anchored on N-doped graphene (Mo_1/N_3-G), where a f_{NRR} of ~40% was realized, denoting its high selectivity for the NRR. Liu *et al.* [66] evaluated a series of SACs supported on g-C_3N_4 (TM@g-C_3N_4) for the NRR, where the f_{NRR} values of Ru@g-C_3N_4 and Rh@g-C_3N_4 reached 97% and 73%, respectively. Li *et al.* [62] estimated the f_{NRR} of Mo-doped graphene-like GaN (Mo@g-GaN), which exhibited a substantial selectivity of ~31% for the NRR. Although the proposed f_{NRR} is an ideal assumption, it can be an effective guide for catalyst design.

However, the experimental FE values for the NRR are usually poor, even when a positive prediction of the NRR selectivity is given by DFT calculations. The main reason for this gap is attributed to the negative electrode potential under working conditions, which greatly promotes H^+ adsorption while exerting a negligible influence on N_2 adsorption [130]. In Fig. 14, the selectivity between the NRR and HER is compared based on the difference between $\Delta G_{N_2^*}$ and ΔG_{H^*}, where nearly one-third of the catalysts exhibit dominant NRR at 0 V *vs.* RHE [41]. However, when the electrode potential is considered, most catalysts are screened out. In particular, the theoretically designed MoB_2 can suppress the HER even at the working potential, and a remarkable FE of 30.84% is experimentally realized. The high NRR selectivity of MoB_2 can be attributed to the enhanced adsorption of N_2 by the modified $Mo^{\delta+}$ sites, as well as the electrostatic repulsion between the $Mo^{\delta+}$ sites and protons. The

Table 1 NRR activity of several typical NRR catalysts mentioned in this review

Catalysts	U_L (V *vs.* RHE)	NH_3 yield (μg h^{-1} mg_{cat}^{-1})	Ref.
V_2-Pc	−0.39	–	[75]
Fe_3-GDY/Gra	−0.37	–	[70]
BN/Ti/N-G	−0.82	–	[78]
Fe-Mo-S	−0.99	–	[80]
Nb-TiO_2(110)	−1.64	21.3	[83]
Fe-MnO_2	−0.58	39.2	[84]
S-Fe_2O_3@PPy	−0.45	22.1	[85]
CrB_3C_1	−0.29	–	[86]
Ru/N_4-C	−0.55	–	[87]
Co-MoS_2	−0.59	0.63 (mmol h^{-1} g^{-1})	[88]
Mo_5N_6(110)	−0.46	–	[89]
W_2N_3	−0.55	11.66 ± 0.98	[90]
s-TiO_2	−0.61	16.67	[91]
Nb_2O_5/C	−0.8	29.1	[92]
$ZrO_2(V_O)$	−0.664	9.63	[93]
Fe_2C	−0.23	–	[94]
Mo@Mo_2CO_2	−0.32	–	[95]
1T-MoS_2	−0.36	71.07	[96]
FeS-V_s	−0.65	–	[97]
NbB_2 NFs	−0.91	30.5	[99]
Au{730}	–	1.648 (μg h^{-1} cm^{-1})	[100]
Pd/C	−1.18	4.5	[101]
Fe_3Si	−0.37	–	[103]
Ru_2MnSi	−0.44	–	[104]
B-graphene	−0.31	–	[110]
C/g-C_3N_4	−0.21	–	[111]
WC(100)	−0.35	–	[46]
Fe/SV-Mo_2N	−0.22	36.4	[116]
$Mo_2C(OH)_2$	−0.62	–	[117]
Mo_1/N_3-G	−0.34	–	[98]
Mo@g-GaN	−0.33	–	[62]
Au NP	−1.13	–	[119]
Au/TiO_2	–	21.4	[120]
Ag_4Ni_2NCs	−0.79	23.32	[121]
Re-Cu(111)-TBE	−0.27	–	[122]
NiSb	−0.78	56.9	[123]
Ru-N_4	−0.16	–	[124]
TiO_2-PEG	–	1.07 (μmol cm^{-2} h^{-1})	[125]
Bi NS	–	13.23	[126]

same is true for the $Mo^{\delta+}$ sites on Fe/SV-Mo_2N, which exhibits a FE value of 17.60% [116].

The thermodynamic suppression strategies also suggest the selection of TMs with weak ΔG_{H^*} in catalyst design, where noble metal catalysts play an important role [119]. For example, Au-based catalysts with high NRR performance have been reported regardless of the structure of stepped facets [100], nanoclusters [120] or alloys [121] due to their ability to inhibit the HER. However, by taking the cost into consideration, Cu in the same group as Au may be a potential substitute. The selec-

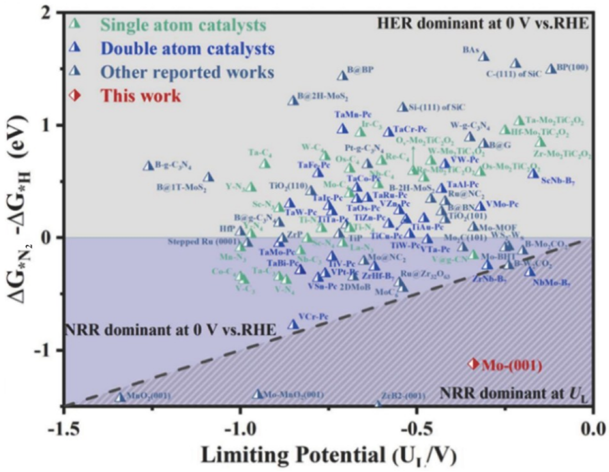

Figure 14 Plot of U_L *versus* the difference between $\Delta G_{N_2^*}$ and ΔG_{H^*} on the reported catalysts. The grey and purple regions represent the HER- and NRR-dominant regions at 0 V *vs.* RHE, respectively. The shaded region represents the NRR-dominant region at the NRR operating potential. Reprinted with permission from Ref. [41]. Copyright 2021, Elsevier.

tivity between the NRR and HER on the twin boundary edge of Cu(111) facets with Re atom doping (denoted as Re-Cu(111)-TBE) was evaluated by DFT calculations [122]. The computed ΔG_{H^*} plus the working potential is −1.01 eV, which is less negative than $\Delta G_{N_2^*}$ = −1.05 eV, showing dominant N_2 adsorption onto the active sites under working conditions. Moreover, the $U_{L\text{-NRR}}$ is much lower than $U_{L\text{-HER}}$ on Re-Cu(111)-TBE. Therefore, Re-Cu(111)-TBE can exhibit high selectivity for the NRR.

Moreover, the NRR selectivity can also be improved by separating the active sites of the NRR and HER (Fig. 15a). Fan *et al.* [123] designed a NiSb catalyst with different active sites for the NRR and HER. As shown in Fig. 15b, the proton prefers to adsorb on the Ni2–Ni3 bridge site of the NiSb surface, while N_2 prefers to adsorb on the Ni1-Sb-Ni2 site. Thus, the active sites of the NRR are no longer limited by the competitive HER, which results in a remarkable FE of 48.00%. On intermetallic Ni_3Mo, the protons prefer to be adsorbed on the Mo–Ni bridge sites, which would not block the active sites for the NRR, i.e., the Mo–Mo bridge sites (Fig. 15c), resulting in a high FE [102].

Kinetic suppression of the HER

There are two well-known reaction mechanisms for the HER, the Volmer-Heyrovsky mechanism and the Volmer-Tafel mechanism, both of which involve the Volmer step, i.e., the formation of H^* on the active sites [115]. In an acidic solution, the Volmer step can directly utilize abundant protons ($H_3O^+ + e^- \rightarrow H^* + H_2O$) and is thus kinetically more favorable than the NRR. Wu *et al.* [124] systematically investigated the kinetic processes of the NRR and HER on Ru-N_4 sites by using grand canonical ensemble DFT (GCE-DFT), which can consider the effects of the electrode potential. The Volmer step on the Ru-N_4 site is shown in Fig. 16a. As the electrode potential decreases, the

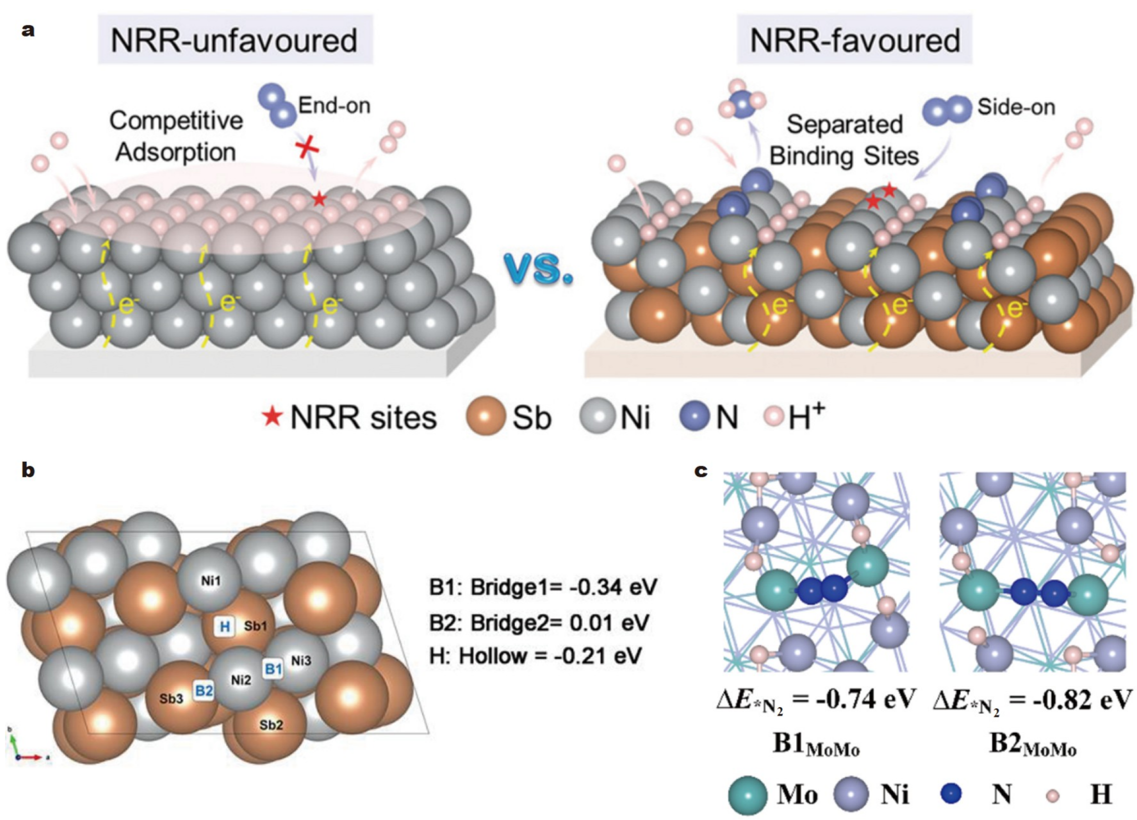

Figure 15 (a) Schematic illustration of the separation of the active sites of the NRR and HER on NiSb alloy. (b) Possible binding sites for protons on NiSb(101) in the top view, along with the corresponding binding energies. Reprinted with permission from Ref. [123]. Copyright 2023, Wiley-VCH. (c) Adsorption configurations and the corresponding binding energies of N_2 on the $B1_{MoMo}$ (left) and $B2_{MoMo}$ (right) sites on the $Ni_3Mo(211)$ surface with full H coverage. Reprinted with permission from Ref. [102]. Copyright 2023, Elsevier.

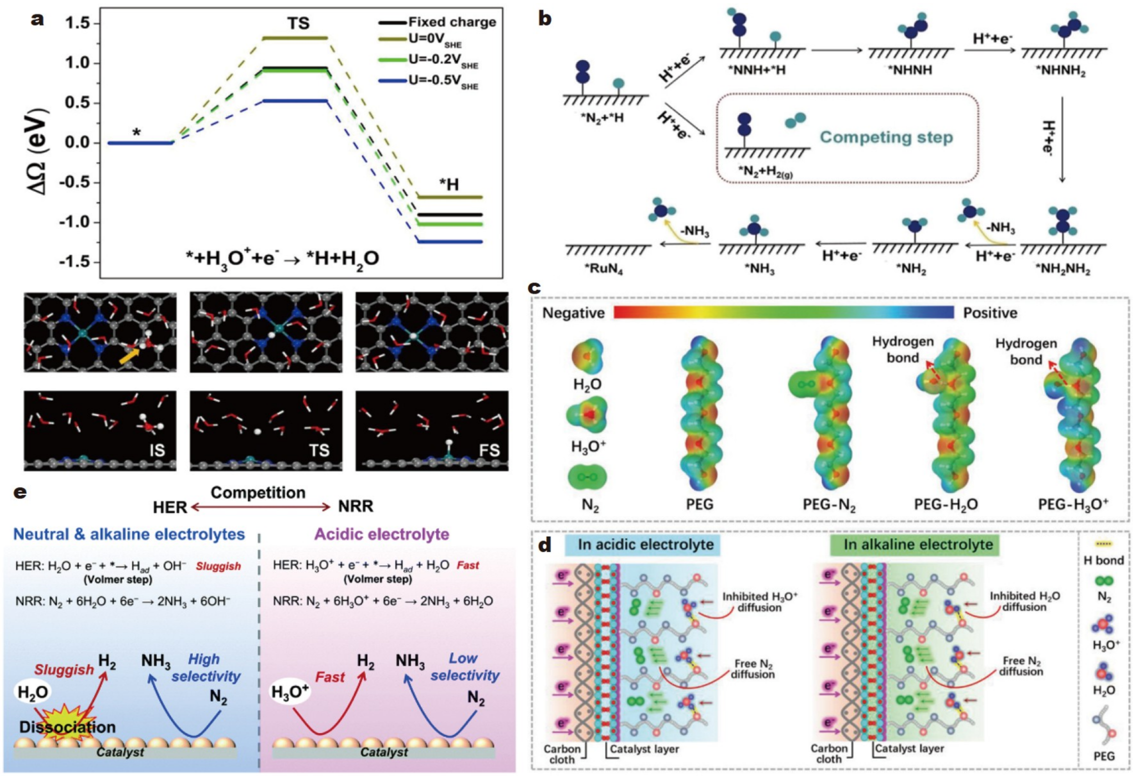

Figure 16 (a) Volmer step on the Ru-N_4 site along with the adsorption configurations. (b) Schematic illustration of the reaction pathway for the NRR. Reprinted with permission from Ref. [124]. Copyright 2022, American Chemical Society. (c) Electrostatic potentials of various molecules in the PEG-containing aqueous electrolyte. (d) Schematic illustrations of the diffusion behaviors of N_2, H_2O and H_3O^+ to the catalyst electrode in PEG400-containing acidic and alkaline electrolytes. Reprinted with permission from Ref. [125]. Copyright 2021, Wiley-VCH. (e) Schematic illustration of the competition between the HER and NRR in different electrolytes. Reprinted with permission from Ref. [115]. Copyright 2021, The Royal Society of Chemistry.

Volmer step becomes both thermodynamically and kinetically more favorable, which explains the poor NRR selectivity. However, since the Ru sites strongly adsorb N_2, the reaction barrier of the Volmer step increases when the active sites are occupied by N_2^*, and the energy barrier of the first hydrogenation step of the NRR decreases (Fig. 16b). The researchers predicted that the kinetic energy barrier of the NRR is 0.16 eV lower than that of the HER when the electrode potential is −0.2 V *vs.* RHE, which accounts for the high FE of 30% experimentally proven for Ru-N_4. This work provides kinetic evidence that dominant N_2 adsorption improves the NRR selectivity.

In the microscopic view, after a catalytic cycle is finished, the active site is prepared to capture a new adsorbate. If there are sufficient protons in the vicinity of the active sites, the proton adsorption will dominate, especially under a relatively negative potential [44]. This will result in a low selectivity for the NRR. In contrast, if there are insufficient protons while a substantial number of N_2 molecules are located around the active sites, then N_2 adsorption will be the dominate process. This will improve the NRR selectivity to some extent, while insufficient protons also delay the hydrogenation steps in the NRR [115]. In this case, regulation of the proton transfer kinetics can guarantee both suppression of proton adsorption and hydrogenation of NRR intermediates. Zhi's group [125] proposed a strategy to regulate the HER kinetics by adding poly(ethylene glycol) (PEG) to the electrolyte. As shown in Fig. 16c, H_2O and H_3O^+, which have asymmetric charges, can form hydrogen bonds with PEG *via* electrostatic interactions. Therefore, when PEG was added to an acidic electrolyte (Fig. 16d), the Volmer step of the HER could be kinetically retarded by the limited H_3O^+ diffusion. In contrast, the binding energy of nonpolar N_2 on PEG is much weaker than those of H_2O and H_3O^+, so N_2 molecules can freely diffuse to the catalyst surface. Moreover, PEG can be added to an alkaline electrolyte, in which the limited H_2O diffusion also suppresses the HER kinetics. By following this strategy, the TiO_2 nanoarray catalyst with a PEG-containing acidic electrolyte experimentally achieved a remarkable NRR FE of 32.13%. To suppress the HER, other H sources can be utilized in the NRR rather than protons. When H^+ has a low availability under neutral or alkaline conditions, the Volmer step will involve water dissociation with sluggish kinetics ($H_2O + e^- \rightarrow H^* + OH^-$), and the NRR selectivity will improve (Fig. 16e) [115,131]. Fortunately, a hydrogen spillover mechanism for the NRR has been developed by directly utilizing the H atom in OH^* species as an H source, and OH^* can be easily recovered from H_2O molecules. Thus, the NRR can readily proceed with limited HER kinetics [116].

Since the Volmer step involves one electron transfer, decreasing the electron availability can also retard the HER kinetics. Singh *et al.* [44] proposed two strategies for limiting the accessibility of electrons: (1) adding an insulator layer between the electrode and the catalyst surface and (2) employing a photochemical method to control the electron flow. Specifically, semimetals with semiconducting features effectively limit the availability of surface electrons. Li *et al.* [126] designed a 2D Bi nanosheet for the NRR whose large charge-transfer resistance effectively limited the electron accessibility of the catalyst surface, with a FE of 10.46%. Notably, the kinetic suppression of the HER also retards the NRR process. Hence, the balance between the NRR selectivity and efficiency should be considered.

STRATEGIES TO ADDRESS OTHER CHALLENGES

There are several other factors that limit the NRR performance beyond the catalyst itself, including the electrolyzer, proton-exchange membrane, and electrolyte. The above issues are discussed in this section.

Electrolytes

Aqueous electrolytes are the most commonly used electrolytes in the electrochemical NRR due to their simplicity, economy, and high fluidity. Nonetheless, aqueous electrolytes exhibit high proton transfer efficiency and thus facilitate the HER, leading to a significant challenge in realizing NRR selectivity. Strategies to modify electrolytes to increase the selectivity for the NRR have been suggested. Adding alkali metal ions to electrolytes can effectively delay the transfer rate of the proton donor due to solvation and steric effects [115]. Hao *et al.* [65] demonstrated that K^+ cations on a Bi catalyst surface restrict proton transfer from the bulk solution to the electrode surface; thus, the active sites are highly accessible to N_2. Moreover, K^+ cations can enhance the NRR activity by decreasing the ΔG of the first NRR step. As a result, an NH_3 yield of 200 mmol g^{-1} h^{-1} and a remarkable FE of 66% is obtained in an aqueous electrolyte under ambient conditions.

It is acknowledged that N_2 suffers from solvation limitations in aqueous electrolytes, with low solubility of 1.98×10^{-3} g per 100 g_{H_2O} at 20°C. Fortunately, this property can be greatly improved in some organic solvent electrolytes. For example, fatty alcohols provide a 30 times higher solubility of N_2 than that in H_2O. However, a proton source to reduce N_2 should be provided if organic solvent electrolytes are used, which are generally composed of some alcohols or H_2O. Kim *et al.* [132] developed ethylenediamine (EDA) as a cathodic solvent for the NRR, with which the Ni catalyst achieved an NH_3 yield of 3.58×10^{-11} mol s^{-1} cm^{-2} and a FE of 17.2%.

The electrolytes in the lithium-mediated NRR (Li-NRR) have also received attention due to their great impact on the performance [133]. Steinberg *et al.* [134] conducted cryogenic transmission electron microscopy to explore the surface phenomena in the Li-NRR. They found that the presence of a proton donor (for example, ethanol) could disrupt the passivation layer, enabling continuous catalytic activity at the Li surface. Cai *et al.* [135] conducted a systematic investigation of ether-based solvents for the Li-NRR by combining molecular dynamics (MD) simulations and experiments. The tetrahydrofuran (THF)-based electrolyte showed a good solvent effect, and Li achieved an impressive FE of 58.5% ± 6.1%. Li *et al.* [136] also reported that adding small amounts of O_2 to the Li-NRR system is beneficial for both the FE and the stability, in which a record high FE of up to 78.0% ± 1.3% is obtained.

Electrolytic cell equipment

At present, more than 90% of reported NRR studies use H-type cells. This type of cell contains a cathode chamber and an anode chamber, which are separated by a proton-exchange membrane. The cathode chamber is assembled with working and reference electrodes, while a counter electrode is set in the anode chamber. The advantage of H-type cells is the ability to control the potential applied to the working electrode, and reactants can be readily added to and separated in the cell. The rational design of electrolytic cell equipment and proton-exchange membranes can further improve the NRR performance. For example, a flow cell would increase the solubility of N_2 in the electrolyte, thereby improving the NRR performance. Fu *et al.* [137] reported that continuous-flow electrolyzer equipment addresses the issue of the low N_2 accessibility of the catalyst. In addition, by combining the hydrogen oxidation reaction (HOR) on the anode, a sustainable hydrogen source for NH_3 synthesis can be provided. Under optimal operation conditions, a FE of up to 61% ± 1% and an energy efficiency of 13% ± 1% at a current density of −6 mA cm^{-2} are achieved.

Electrolyzer design could also improve the NRR selectivity. For instance, the back-to-back cell may have a natural ability to suppress the HER since there is a dense membrane separating the two chambers, which can control the proton source supply [138]. This increases the N_2 accessibility of active sites, thus improving the NRR selectivity. Following this strategy, Renner *et al.* [139] developed a back-to-back cell for the NRR, where the Fe-based catalyst realized an ultrahigh FE of 41%.

Membrane design is essential for accurate NH_3 detection. The Nafion membrane is the most common membrane used to separate the cathode and anode chambers, as it can adsorb and release NH_3, affecting the NH_3 quantitation in the NRR. Liu *et al.* [140] performed a series of experiments to examine different membranes for the NRR with Pd nanosheets as catalysts. They discovered that the Celgard 3501 membrane exhibited the lowest adsorption and release of NH_3. To more accurately evaluate the NRR activity, Ren *et al.* [141] proposed that the Nafion membrane be replaced by a salt bridge.

CONCLUSIONS AND OUTLOOK

The electrochemical NRR is not only an environmentally friendly alternative to the energy-intensive Haber-Bosch method but also a promising technique for the utilization and storage of renewable sources. In the near future, there are green prospects for the widespread use of distributed electrochemical NH_3 production devices powered by renewable energy. It is well acknowledged that catalysts account for most of the cost of the electrochemical NRR, but their catalytic performance is still unsatisfactory due to their low activity and selectivity. Thus, high-efficiency NRR catalysts are urgently required. In particular, DFT calculation is a powerful tool to assist in catalyst design, which provides fundamental insights into the catalytic mechanism and an understanding of the structure-performance relationship. We believe that DFT calculations will guide the development of NRR catalysts and accelerate the wide application of the electrochemical NRR.

However, there is still a nonnegligible gap between the calculations and experiments. To achieve more practical results, several aspects of DFT calculations should be further considered: (1) Since the reaction rate directly depends on the kinetics, developing an advanced kinetic model would be very helpful for accurately predicting the NRR performance. (2) A precise description of the electronic structure is very important to understand the "acceptance-donation" mechanism for N_2 activation, which requires good matching between the frontier orbitals. Therefore, a view of the suborbitals should be obtained to determine the electronic interactions. (3) The effects of the electrode potential and electrolyte should be considered since they greatly affect the catalytic behavior during the NRR process. It is known that the present computational capabilities cannot fully simulate the real reaction situations of the NRR; thus, there will always be a trade-off between unlimited model size and limited computational resources. At this stage, we strongly propose performing proof-of-concept experiments to verify the DFT results, which is very meaningful for further development of material design.

Received 10 December 2023; accepted 1 March 2024; published online 19 March 2024

1 MacFarlane DR, Cherepanov PV, Choi J, *et al.* A roadmap to the ammonia economy. Joule, 2020, 4: 1186–1205
2 Tang C, Qiao SZ. How to explore ambient electrocatalytic nitrogen reduction reliably and insightfully. Chem Soc Rev, 2019, 48: 3166–3180
3 Smil V. Detonator of the population explosion. Nature, 1999, 400: 415
4 Erisman JW, Sutton MA, Galloway J, *et al.* How a century of ammonia synthesis changed the world. Nat Geosci, 2008, 1: 636–639
5 Foster SL, Bakovic SIP, Duda RD, *et al.* Catalysts for nitrogen reduction to ammonia. Nat Catal, 2018, 1: 490–500
6 Deng J, Iñiguez JA, Liu C. Electrocatalytic nitrogen reduction at low temperature. Joule, 2018, 2: 846–856
7 Guo J, Chen P. Catalyst: NH_3 as an Energy Carrier. Chem, 2017, 3: 709–712
8 Zhao Y, Setzler BP, Wang J, *et al.* An efficient direct ammonia fuel cell for affordable carbon-neutral transportation. Joule, 2019, 3: 2472–2484
9 Klerke A, Christensen CH, Nørskov JK, *et al.* Ammonia for hydrogen storage: Challenges and opportunities. J Mater Chem, 2008, 18: 2304
10 Chen JG, Crooks RM, Seefeldt LC, *et al.* Beyond fossil fuel-driven nitrogen transformations. Science, 2018, 360: eaar6611
11 Martín AJ, Shinagawa T, Pérez-Ramírez J. Electrocatalytic reduction of nitrogen: From Haber-Bosch to ammonia artificial leaf. Chem, 2019, 5: 263–283
12 Cheng H, Ding LX, Chen GF, *et al.* Molybdenum carbide nanodots enable efficient electrocatalytic nitrogen fixation under ambient conditions. Adv Mater, 2018, 30: e1803694
13 Qing G, Ghazfar R, Jackowski ST, *et al.* Recent advances and challenges of electrocatalytic N_2 reduction to ammonia. Chem Rev, 2020, 120: 5437–5516
14 Giddey S, Badwal SPS, Munnings C, *et al.* Ammonia as a renewable energy transportation media. ACS Sustain Chem Eng, 2017, 5: 10231–10239
15 Olabi AG, bahri A, Abdelghafar AA, *et al.* Large-vscale hydrogen production and storage technologies: Current status and future directions. Int J Hydrogen Energy, 2021, 46: 23498–23528
16 Singstock NR, Musgrave CB. How the bioinspired $Fe_2Mo_6S_8$ Chevrel breaks electrocatalytic nitrogen reduction scaling relations. J Am Chem Soc, 2022, 144: 12800–12806
17 Yao Y, Zhu S, Wang H, *et al.* A spectroscopic study on the nitrogen electrochemical reduction reaction on gold and platinum surfaces. J Am Chem Soc, 2018, 140: 1496–1501
18 Chen A, Xia BY. Ambient dinitrogen electrocatalytic reduction for ammonia synthesis. J Mater Chem A, 2019, 7: 23416–23431
19 Deutch J. Is net zero carbon 2050 possible? Joule, 2020, 4: 2237–2240
20 Soloveichik G. Electrochemical synthesis of ammonia as a potential alternative to the Haber-Bosch process. Nat Catal, 2019, 2: 377–380
21 Wang L, Xia M, Wang H, *et al.* Greening ammonia toward the solar ammonia refinery. Joule, 2018, 2: 1055–1074
22 Dinh CT, Jain A, de Arquer FPG, *et al.* Multi-site electrocatalysts for hydrogen evolution in neutral media by destabilization of water molecules. Nat Energy, 2018, 4: 107–114
23 Cheng H, Cui P, Wang F, *et al.* High efficiency electrochemical nitrogen fixation achieved with a lower pressure reaction system by changing the chemical equilibrium. Angew Chem Int Ed, 2019, 58: 15541–15547
24 Chen BWJ, Xu L, Mavrikakis M. Computational methods in heterogeneous catalysis. Chem Rev, 2021, 121: 1007–1048
25 Daw P, Ben-David Y, Milstein D. Acceptorless dehydrogenative coupling using ammonia: Direct synthesis of N-heteroaromatics from diols catalyzed by ruthenium. J Am Chem Soc, 2018, 140: 11931–11934
26 Chen ZW, Chen LX, Wen Z, *et al.* Understanding electro-catalysis by using density functional theory. Phys Chem Chem Phys, 2019, 21: 23782–23802
27 Zhao X, Levell ZH, Yu S, *et al.* Atomistic understanding of two-dimensional electrocatalysts from first principles. Chem Rev, 2022, 122: 10675–10709
28 Tian D, Denny SR, Li K, *et al.* Density functional theory studies of transition metal carbides and nitrides as electrocatalysts. Chem Soc Rev, 2021, 50: 12338–12376
29 Bhandari S, Rangarajan S, Mavrikakis M. Combining computational modeling with reaction kinetics experiments for elucidating the *in situ* nature of the active site in catalysis. Acc Chem Res, 2020, 53: 1893–1904
30 Liu B, Liu J, Xin L, *et al.* Unraveling reactivity descriptors and structure sensitivity in low-temperature NH_3-SCR reaction over Ce-TiO_x catalysts: A combined computational and experimental study. ACS Catal, 2021, 11: 7613–7636
31 Ziemba M, Schilling C, Ganduglia-Pirovano MV, *et al.* Toward an atomic-level understanding of ceria-based catalysts: When experiment and theory go hand in hand. Acc Chem Res, 2021, 54: 2884–2893
32 Zhang L, Ji X, Ren X, *et al.* Electrochemical ammonia synthesis *via* nitrogen reduction reaction on a MoS_2 catalyst: Theoretical and experimental studies. Adv Mater, 2018, 30: e1800191
33 Li XF, Li QK, Cheng J, *et al.* Conversion of dinitrogen to ammonia by FeN_3-embedded graphene. J Am Chem Soc, 2016, 138: 8706–8709
34 An Q, Shen Y, Fortunelli A, *et al.* QM-mechanism-based hierarchical high-throughput in silico screening catalyst design for ammonia synthesis. J Am Chem Soc, 2018, 140: 17702–17710
35 Liu JC, Ma XL, Li Y, *et al.* Heterogeneous Fe_3 single-cluster catalyst for ammonia synthesis *via* an associative mechanism. Nat Commun, 2018, 9: 1610
36 Ohki Y, Munakata K, Matsuoka Y, *et al.* Nitrogen reduction by the Fe sites of synthetic $[Mo_3S_4Fe]$ cubes. Nature, 2022, 607: 86–90
37 Rod TH, Logadottir A, Nørskov JK. Ammonia synthesis at low temperatures. J Chem Phys, 2000, 112: 5343–5347
38 Kordali V, Kyriacou G, Lambrou C. Electrochemical synthesis of ammonia at atmospheric pressure and low temperature in a solid polymer electrolyte cell. Chem Commun, 2000, 17: 1673–1674
39 Logadóttir Á, Nørskov JK. Ammonia synthesis over a Ru(0001) surface studied by density functional calculations. J Catal, 2003, 220: 273–279
40 Skúlason E, Bligaard T, Gudmundsdóttir S, *et al.* A theoretical evaluation of possible transition metal electro-catalysts for N_2 reduction. Phys Chem Chem Phys, 2012, 14: 1235–1245
41 Zhou HY, Qu YB, Li JC, *et al.* Effectively boosting selective ammonia synthesis on electron-deficient surface of MoB_2. Appl Catal B-Environ, 2022, 305: 121023
42 Shi L, Yin Y, Wang S, *et al.* Rational catalyst design for N_2 reduction under ambient conditions: Strategies toward enhanced conversion efficiency. ACS Catal, 2020, 10: 6870–6899
43 van der Ham CJM, Koper MTM, Hetterscheid DGH. Challenges in reduction of dinitrogen by proton and electron transfer. Chem Soc Rev, 2014, 43: 5183–5191
44 Singh AR, Rohr BA, Schwalbe JA, *et al.* Electrochemical ammonia synthesis—The selectivity challenge. ACS Catal, 2016, 7: 706–709
45 Zhao X, Hu G, Chen GF, *et al.* Comprehensive understanding of the thriving ambient electrochemical nitrogen reduction reaction. Adv Mater, 2021, 33: e2007650
46 Ellingsson V, Iqbal A, Skúlason E, *et al.* Nitrogen reduction reaction to ammonia on transition metal carbide catalysts. ChemSusChem, 2023, 16: e202300947
47 Abghoui Y, Garden AL, Howalt JG, *et al.* Electroreduction of N_2 to

ammonia at ambient conditions on mononitrides of Zr, Nb, Cr, and V: A DFT guide for experiments. ACS Catal, 2015, 6: 635–646
48 Ling C, Zhang Y, Li Q, *et al.* New mechanism for N_2 reduction: The essential role of surface hydrogenation. J Am Chem Soc, 2019, 141: 18264–18270
49 Cui X, Tang C, Zhang Q. A review of electrocatalytic reduction of dinitrogen to ammonia under ambient conditions. Adv Energy Mater, 2018, 8: 1800369
50 Ma XL, Liu JC, Xiao H, *et al.* Surface single-cluster catalyst for N_2-to-NH_3 thermal conversion. J Am Chem Soc, 2018, 140: 46–49
51 Jia HP, Quadrelli EA. Mechanistic aspects of dinitrogen cleavage and hydrogenation to produce ammonia in catalysis and organometallic chemistry: Relevance of metal hydride bonds and dihydrogen. Chem Soc Rev, 2014, 43: 547–564
52 Chen Z, Liu C, Sun L, *et al.* Progress of experimental and computational catalyst design for electrochemical nitrogen fixation. ACS Catal, 2022, 12: 8936–8975
53 Anderson JS, Rittle J, Peters JC. Catalytic conversion of nitrogen to ammonia by an iron model complex. Nature, 2013, 501: 84–87
54 Tayyebi E, Abghoui Y, Skúlason E. Elucidating the mechanism of electrochemical N_2 reduction at the Ru(0001) electrode. ACS Catal, 2019, 9: 11137–11145
55 Légaré MA, Bélanger-Chabot G, Dewhurst RD, *et al.* Nitrogen fixation and reduction at boron. Science, 2018, 359: 896–900
56 Ling C, Niu X, Li Q, *et al.* Metal-free single atom catalyst for N_2 fixation driven by visible light. J Am Chem Soc, 2018, 140: 14161–14168
57 Fan Y, Yu J, Song X, *et al.* The role of sp-hybridized boron atoms in the highly efficient photocatalytic N_2 reduction activity of boron-doped triphenylene-graphdiyne. J Mater Chem A, 2021, 9: 26077–26085
58 Dai T, Lang X, Wang Z, *et al.* Rational design of an Fe cluster catalyst for robust nitrogen activation. J Mater Chem A, 2021, 9: 21219–21227
59 Chen ZW, Yan J, Jiang Q. Single or double: Which is the altar of atomic catalysts for nitrogen reduction reaction? Small Methods, 2019, 3: 1800291
60 Montoya JH, Tsai C, Vojvodic A, *et al.* The challenge of electrochemical ammonia synthesis: A new perspective on the role of nitrogen scaling relations. ChemSusChem, 2015, 8: 2180–2186
61 Suryanto BHR, Wang D, Azofra LM, *et al.* MoS_2 polymorphic engineering enhances selectivity in the electrochemical reduction of nitrogen to ammonia. ACS Energy Lett, 2019, 4: 430–435
62 Li L, Martirez JMP, Carter EA. Prediction of highly selective electrocatalytic nitrogen reduction at low overpotential on a Mo-doped g-GaN monolayer. ACS Catal, 2020, 10: 12841–12857
63 Pang Y, Su C, Jia G, *et al.* Emerging two-dimensional nanomaterials for electrochemical nitrogen reduction. Chem Soc Rev, 2021, 50: 12744–12787
64 Liu S, Qian T, Wang M, *et al.* Proton-filtering covalent organic frameworks with superior nitrogen penetration flux promote ambient ammonia synthesis. Nat Catal, 2021, 4: 322–331
65 Hao YC, Guo Y, Chen LW, *et al.* Promoting nitrogen electroreduction to ammonia with bismuth nanocrystals and potassium cations in water. Nat Catal, 2019, 2: 448–456
66 Liu X, Jiao Y, Zheng Y, *et al.* Building up a picture of the electrocatalytic nitrogen reduction activity of transition metal single-atom catalysts. J Am Chem Soc, 2019, 141: 9664–9672
67 Jiao S, Fu X, Huang H. Descriptors for the evaluation of electrocatalytic reactions: d-band theory and beyond. Adv Funct Mater, 2021, 32: 2107651
68 Chen ZW, Chen LX, Yang CC, *et al.* Atomic (single, double, and triple atoms) catalysis: Frontiers, opportunities, and challenges. J Mater Chem A, 2019, 7: 3492–3515
69 Jin H, Guo C, Liu X, *et al.* Emerging two-dimensional nanomaterials for electrocatalysis. Chem Rev, 2018, 118: 6337–6408
70 Chen ZW, Chen LX, Jiang M, *et al.* A triple atom catalyst with ultrahigh loading potential for nitrogen electrochemical reduction. J Mater Chem A, 2020, 8: 15086–15093
71 Mounet N, Gibertini M, Schwaller P, *et al.* Two-dimensional materials from high-throughput computational exfoliation of experimentally known compounds. Nat Nanotech, 2018, 13: 246–252
72 Fei H, Dong J, Chen D, *et al.* Single atom electrocatalysts supported on graphene or graphene-like carbons. Chem Soc Rev, 2019, 48: 5207–5241
73 Mahmood J, Lee EK, Jung M, *et al.* Nitrogenated holey two-dimensional structures. Nat Commun, 2015, 6: 6486
74 Sun CN, Wang ZL, Lang XY, *et al.* Synergistic effect of active sites of double-atom catalysts for nitrogen reduction reaction. ChemSusChem, 2021, 14: 4593–4600
75 Guo X, Gu J, Lin S, *et al.* Tackling the activity and selectivity challenges of electrocatalysts toward the nitrogen reduction reaction *via* atomically dispersed biatom catalysts. J Am Chem Soc, 2020, 142: 5709–5721
76 Hui L, Xue Y, Yu H, *et al.* Highly efficient and selective generation of ammonia and hydrogen on a graphdiyne-based catalyst. J Am Chem Soc, 2019, 141: 10677–10683
77 Deng J, Deng D, Bao X. Robust catalysis on 2D materials encapsulating metals: Concept, application, and perspective. Adv Mater, 2017, 29: 1606967
78 Tang S, Dang Q, Liu T, *et al.* Realizing a not-strong-not-weak polarization electric field in single-atom catalysts sandwiched by boron nitride and graphene sheets for efficient nitrogen fixation. J Am Chem Soc, 2020, 142: 19308–19315
79 Lin G, Ju Q, Guo X, *et al.* Intrinsic electron localization of metastable MoS_2 boosts electrocatalytic nitrogen reduction to ammonia. Adv Mater, 2021, 33: e2007509
80 Azofra LM, Sun C, Cavallo L, *et al.* Feasibility of N_2 binding and reduction to ammonia on Fe-deposited MoS_2 2D sheets: A DFT study. Chem Eur J, 2017, 23: 8275–8279
81 Luo Y, Chen GF, Ding L, *et al.* Efficient electrocatalytic N_2 fixation with MXene under ambient conditions. Joule, 2019, 3: 279–289
82 Yao X, Chen Z, Wang Y, *et al.* Activated basal planes of WS_2 by intrinsic defects as catalysts for the electrocatalytic nitrogen reduction reaction. J Mater Chem A, 2019, 7: 25961–25968
83 Gao Y, Yang Y, Hao L, *et al.* Single Nb atom modified anatase TiO_2 (110) for efficient electrocatalytic nitrogen reduction reaction. Chem Catal, 2022, 2: 2275–2288
84 Huang T, Liu Z, Zhang Y, *et al.* Promoting electrocatalytic nitrogen reduction to ammonia *via* Fe-boosted nitrogen activation on MnO_2 surfaces. J Mater Chem A, 2020, 8: 13679–13684
85 Jin F, Yin H, Feng R, *et al.* Charge transfer and vacancy engineering of Fe_2O_3 nanoparticle catalysts for highly selective N_2 reduction towards NH_3 synthesis. J Colloid Interface Sci, 2023, 647: 354–363
86 Zafari M, Kumar D, Umer M, *et al.* Machine learning-based high throughput screening for nitrogen fixation on boron-doped single atom catalysts. J Mater Chem A, 2020, 8: 5209–5216
87 Chen ZW, Lu Z, Chen LX, *et al.* Machine-learning-accelerated discovery of single-atom catalysts based on bidirectional activation mechanism. Chem Catal, 2021, 1: 183–195
88 Zhang J, Tian X, Liu M, *et al.* Cobalt-modulated molybdenum-dinitrogen interaction in MoS_2 for catalyzing ammonia synthesis. J Am Chem Soc, 2019, 141: 19269–19275
89 Kong Y, He T, Puente Santiago AR, *et al.* Unravelling the reaction mechanisms of N_2 fixation on molybdenum nitride: A full DFT study from the pristine surface to heteroatom anchoring. ChemSusChem, 2021, 14: 3257–3266
90 Jin H, Li L, Liu X, *et al.* Nitrogen vacancies on 2D layered W_2N_3: A stable and efficient active site for nitrogen reduction reaction. Adv Mater, 2019, 31: 1902709
91 Li P, Jin Z, Fang Z, *et al.* A surface-strained and geometry-tailored nanoreactor that promotes ammonia electrosynthesis. Angew Chem Int Ed, 2020, 59: 22610–22616
92 Zhang M, Yin H, Jin F, *et al.* Vacancy engineering of oxidized Nb_2CT_x MXenes for a biased nitrogen fixation. Green Energy Environ, 2023, 8: 1185–1194
93 Xia J, Guo H, Cheng M, *et al.* Electrospun zirconia nanofibers for enhancing the electrochemical synthesis of ammonia by artificial nitrogen fixation. J Mater Chem A, 2021, 9: 2145–2151

94 Wang S, Li B, Li L, *et al.* Highly efficient N_2 fixation catalysts: Transition-metal carbides M_2C (MXenes). Nanoscale, 2020, 12: 538–547
95 Huang B, Li N, Ong WJ, *et al.* Single atom-supported MXene: How single-atomic-site catalysts tune the high activity and selectivity of electrochemical nitrogen fixation. J Mater Chem A, 2019, 7: 27620–27631
96 Liu R, Guo T, Fei H, *et al.* Highly efficient electrocatalytic N_2 reduction to ammonia over metallic 1T phase of MoS_2 enabled by active sites separation mechanism. Adv Sci, 2022, 9: 2103583
97 Yin H, Du A. Boosting nitrogen reduction activity by defect engineering in 2D iron monochalcogenides FeX (X = S, Se). Small Struct, 2022, 3: 2200107
98 Zhao W, Zhang L, Luo Q, *et al.* Single $Mo_1(Cr_1)$ atom on nitrogen-doped graphene enables highly selective electroreduction of nitrogen into ammonia. ACS Catal, 2019, 9: 3419–3425
99 Feng R, Yin H, Jin F, *et al.* Highly selective N_2 electroreduction to NH_3 using a boron-vacancy-rich diatomic NbB catalyst. Small, 2023, 19: 2301627
100 Bao D, Zhang Q, Meng FL, *et al.* Electrochemical reduction of N_2 under ambient conditions for artificial N_2 fixation and renewable energy storage using N_2/NH_3 cycle. Adv Mater, 2017, 29: 1604799
101 Wang J, Yu L, Hu L, *et al.* Ambient ammonia synthesis *via* palladium-catalyzed electrohydrogenation of dinitrogen at low overpotential. Nat Commun, 2018, 9: 1795
102 Zhou HY, Qu YB, Fan YC, *et al.* Multi-site intermetallic Ni_3Mo effectively boosts selective ammonia synthesis. Appl Catal B-Environ, 2023, 339: 123133
103 Yin H, Bell S, Golberg D, *et al.* Enhancing the nitrogen reduction activity of iron with inactive group-IVA elements at optimized stoichiometry. Inorg Chem Front, 2023, 10: 4442–4449
104 Yin H, Du A. Revealing the potential of ternary medium-entropy alloys as exceptional electrocatalysts toward nitrogen reduction: An example of Heusler alloys. ACS Appl Mater Interfaces, 2022, 14: 15235–15242
105 Hannagan RT, Giannakakis G, Flytzani-Stephanopoulos M, *et al.* Single-atom alloy catalysis. Chem Rev, 2020, 120: 12044–12088
106 Greiner MT, Jones TE, Beeg S, *et al.* Free-atom-like d states in single-atom alloy catalysts. Nat Chem, 2018, 10: 1008–1015
107 Dai T, Wang Z, Lang X, *et al.* "Sabatier principle" of d electron number for describing the nitrogen reduction reaction performance of single-atom alloy catalysts. J Mater Chem A, 2022, 10: 16900–16907
108 Zhang Y, Li S, Sun C, *et al.* Understanding and modifying the scaling relations for ammonia synthesis on dilute metal alloys: From single-atom alloys to dimer alloys. ACS Catal, 2022, 12: 9201–9212
109 Yu X, Han P, Wei Z, *et al.* Boron-doped graphene for electrocatalytic N_2 reduction. Joule, 2018, 2: 1610–1622
110 Liu C, Li Q, Wu C, *et al.* Single-boron catalysts for nitrogen reduction reaction. J Am Chem Soc, 2019, 141: 2884–2888
111 Li H, Yang L, Wang Z, *et al.* N-heterocyclic carbene as a promising metal-free electrocatalyst with high efficiency for nitrogen reduction to ammonia. J Energy Chem, 2020, 46: 78–86
112 Wen L, Sun K, Liu X, *et al.* Electronic state and microenvironment modulation of metal nanoparticles stabilized by MOFs for boosting electrocatalytic nitrogen reduction. Adv Mater, 2023, 35: 2210669
113 Ling C, Ouyang Y, Li Q, *et al.* A general two-step strategy-based high-throughput screening of single atom catalysts for nitrogen fixation. Small Methods, 2019, 3: 1800376
114 Liu D, Chen M, Du X, *et al.* Development of electrocatalysts for efficient nitrogen reduction reaction under ambient condition. Adv Funct Mater, 2021, 31: 2008983
115 Ren Y, Yu C, Tan X, *et al.* Strategies to suppress hydrogen evolution for highly selective electrocatalytic nitrogen reduction: Challenges and perspectives. Energy Environ Sci, 2021, 14: 1176–1193
116 Sun CN, Qu YB, Wang ZL, *et al.* Hydrogen spillover in alkaline solutions for effective nitrogen fixation. Chem Eng J, 2023, 471: 144589
117 Lv X, Kou L, Frauenheim T. Hydroxyl-boosted nitrogen reduction reaction: The essential role of surface hydrogen in functionalized MXenes. ACS Appl Mater Interfaces, 2021, 13: 14283–14290
118 Wang T, Abild-Pedersen F. Achieving industrial ammonia synthesis rates at near-ambient conditions through modified scaling relations on a confined dual site. Proc Natl Acad Sci USA, 2021, 118: e2106527118
119 Xue ZH, Zhang SN, Lin YX, *et al.* Electrochemical reduction of N_2 into NH_3 by donor-acceptor couples of Ni and Au nanoparticles with a 67.8% faradaic efficiency. J Am Chem Soc, 2019, 141: 14976–14980
120 Shi MM, Bao D, Wulan BR, *et al.* Au sub-nanoclusters on TiO_2 toward highly efficient and selective electrocatalyst for N_2 conversion to NH_3 at ambient conditions. Adv Mater, 2017, 29: 1606550
121 Han M, Guo M, Yun Y, *et al.* Effect of heteroatom and charge reconstruction in atomically precise metal nanoclusters on electrochemical synthesis of ammonia. Adv Funct Mater, 2022, 32: 2202820
122 Dai T, Wang Z, Wen Z, *et al.* Tailoring electronic structure of copper twin boundaries toward highly efficient nitrogen reduction reaction. ChemSusChem, 2022, 15: e202201189
123 Fan G, Xu W, Li J, *et al.* Nanoporous NiSb to enhance nitrogen electroreduction *via* tailoring competitive adsorption sites. Adv Mater, 2021, 33: e2101126
124 Wu T, Melander MM, Honkala K. Coadsorption of NRR and HER intermediates determines the performance of Ru-N_4 toward electrocatalytic N_2 reduction. ACS Catal, 2022, 12: 2505–2512
125 Guo Y, Gu J, Zhang R, *et al.* Molecular crowding effect in aqueous electrolytes to suppress hydrogen reduction reaction and enhance electrochemical nitrogen reduction. Adv Energy Mater, 2021, 11: 2101699
126 Li L, Tang C, Xia B, *et al.* Two-dimensional mosaic bismuth nanosheets for highly selective ambient electrocatalytic nitrogen reduction. ACS Catal, 2019, 9: 2902–2908
127 Li Z, Fu JY, Feng Y, *et al.* A silver catalyst activated by stacking faults for the hydrogen evolution reaction. Nat Catal, 2019, 2: 1107–1114
128 Chen D, Pu Z, Wang P, *et al.* Mapping hydrogen evolution activity trends of intermetallic Pt-group silicides. ACS Catal, 2022, 12: 2623–2631
129 Kong Y, Li Y, Sang X, *et al.* Atomically dispersed zinc(I) active sites to accelerate nitrogen reduction kinetics for ammonia electrosynthesis. Adv Mater, 2021, 34: e2103548
130 Choi C, Gu GH, Noh J, *et al.* Understanding potential-dependent competition between electrocatalytic dinitrogen and proton reduction reactions. Nat Commun, 2021, 12: 4353
131 McCrum IT, Koper MTM. The role of adsorbed hydroxide in hydrogen evolution reaction kinetics on modified platinum. Nat Energy, 2020, 5: 891–899
132 Kim K, Yoo CY, Kim JN, *et al.* Electrochemical synthesis of ammonia from water and nitrogen in ethylenediamine under ambient temperature and pressure. J Electrochem Soc, 2016, 163: F1523–F1526
133 Lazouski N, Steinberg KJ, Gala ML, *et al.* Proton donors induce a differential transport effect for selectivity toward ammonia in lithium-mediated nitrogen reduction. ACS Catal, 2022, 12: 5197–5208
134 Steinberg K, Yuan X, Klein CK, *et al.* Imaging of nitrogen fixation at lithium solid electrolyte interphases *via* cryo-electron microscopy. Nat Energy, 2022, 8: 138–148
135 Cai X, Li X, You J, *et al.* Lithium-mediated ammonia electrosynthesis with ether-based electrolytes. J Am Chem Soc, 2023, 145: 25716–25725
136 Li K, Andersen SZ, Statt MJ, *et al.* Enhancement of lithium-mediated ammonia synthesis by addition of oxygen. Science, 2021, 374: 1593–1597
137 Fu X, Pedersen JB, Zhou Y, *et al.* Continuous-flow electrosynthesis of ammonia by nitrogen reduction and hydrogen oxidation. Science, 2023, 379: 707–712
138 Chen G, Ren S, Zhang L, *et al.* Advances in electrocatalytic N_2 reduction—Strategies to tackle the selectivity challenge. Small Methods, 2019, 3: 1800337
139 Renner JN, Greenlee LF, Ayres KE, *et al.* Electrochemical synthesis of ammonia: A low pressure, low temperature approach. Interface Mag, 2015, 24: 51–57
140 Liu H, Zhang Y, Luo J. The removal of inevitable NO species in catalysts and the selection of appropriate membrane for measuring electrocatalytic ammonia synthesis accurately. J Energy Chem, 2020,

49: 51–58
141 Ren Y, Yu C, Tan X, *et al.* Is it appropriate to use the nafion membrane in electrocatalytic N_2 reduction? Small Methods, 2019, 3: 1900474

Acknowledgements This work was supported by the National Natural Science Foundation of China (21673095).

Author contributions Jiang Q supervised the project and conceived the idea. Dai TY wrote the draft. Yang CC revised the manuscript and provided constructive suggestions. All authors discussed and commented on the manuscript.

Conflict of interest These authors declared no conflict of interest.

Tian-Yi Dai received his BE and PhD degrees from Jilin University in 2018 and 2023, respectively. He is currently working as a postdoctoral fellow at the School of Materials Science and Engineering, Jilin University. His current research focuses on the catalyst design through density functional theory calculations. Some of his studies are carried out in close collaboration with experiments.

Chun-Cheng Yang received his BSc and PhD degrees from Jilin University in 2001 and 2006, respectively. He is currently working as a professor at the School of Materials Science and Engineering, Jilin University. He had worked as a postdoctoral fellow at The University of New South Wales and The University of Sydney for 7 years. His research interests focus on micro- and nano-scale energy materials.

Qing Jiang obtained his PhD degree in chemistry from the University of Stuttgart, Germany in 1990. Since 1992, he has been a professor at the School of Materials Science and Engineering, Jilin University, China. His research interests focus on the synthesis of nanomaterials as well as their applications in catalysis, energy storage and conversion, and interface thermodynamics and kinetics of nanomaterials.

密度泛函理论在氮还原反应催化剂设计中的应用进展

代天一, 杨春成*, 蒋青*

摘要 发展电化学氮气还原反应(NRR)的合成氨技术可以有效缓解工业上的哈伯-博什法合成氨的化石燃料消耗与碳排放问题. 同时, 氨是一种无碳的能源载体, NRR可以实现可再生能源的转换, 因此具有广阔的发展前景. 然而, 高效催化剂的缺乏限制了NRR技术的发展. 为此, 人们对开发高效催化剂进行了广泛的探索, 其中密度泛函理论(DFT)计算在辅助催化剂设计方面发挥了重要作用. 在本综述中, 我们总结了最近的催化剂设计策略, 这些策略的目的是提高NRR的催化活性和选择性. 此外, 本综述还回顾了具有代表性的计算工作, 并对进一步改善催化性能提出了见解. 最后, 本综述简要讨论了通过DFT计算进行催化剂设计所面临的挑战和机遇. 目的在于指导人们采用更有效的设计策略来实现高效的NRR过程.

